THE UNIVERSITY OF CHICAGO

MOLECULAR MODELING OF BLOCK COPOLYMER LITHOGRAPHY: THERMODYNAMIC AND KINETIC ASPECTS OF GRAPHOEPITAXY AND CHEMOEPITAXY.

A DISSERTATION SUBMITTED TO
THE FACULTY OF THE INSTITUTE FOR MOLECULAR ENGINEERING
IN CANDIDACY FOR THE DEGREE OF
DOCTOR OF PHILOSOPHY

BY
BRANDON LOUIS PETERS

CHICAGO, ILLINOIS
DECEMBER 2016

To Randy L. Peters

For me, it is far better to grasp the Universe as it really is than to persist in delusion, however satisfying and reassuring.

—Carl Sagan, *The Demon-Haunted World: Science as a Candle in the Dark*

TABLE OF CONTENTS

LIST OF FIGURES

ACKNOWLEDGMENTS

Throughout my life, I have been lucky enough to have great family and friends that have supported from my home town of Ankeny, Iowa and across the world.

First and foremost, I want to thank my doctoral advisor Prof. Juan de Pablo for his support and advice throughout my career as a graduate student. He's helped me grow as a person and a scientist, and he has given me multiple opportunities to learn and experience the life of different types of research, through my internship at Tokyo Electron America and at Sandia National Labs. During my graduate school career, I have struggled, but Professor de Pablo's advice and determination to make the best scientist I could possibly be is greatly appreciated.

When I first joined the Chemical Engineering department at the University of Wisconsin-Madison, I worked closely with Dr. Abelardo Ramirez-Hernandez, Dr. Gregory Toepperwein, Professor Su-mi Hur, Professor Jian Qin, Dr. Gurdaman Khaira, Professor Jonathan K. Whitmer, and Dr. Darin Pike. These great colleagues helped me understand the basics of polymer science and computer simulations. Without their help and tolerance of my constant questioning and stubborn attitude, I would not be here today. A special thanks to Abelardo, Su-mi and Jian for proof reading my papers, helping me debug, and discussions of ideas and theories.

The most important part of graduate school is the learning, but growing as a person and finding new friends is also important. Through my time at the University of Wisconsin-Madison and the University of Chicago, I have met a lot of great friends. Without their support and friendship, I would not be in the position to write this thesis. I specifically want to thank Dr. Aaron Fluit, Dr. Tyler Robers, Grant Garner, Dr. Kevin Schulte, Matthew Wang, Josh Lequieu, Lucas Antony, Dr. Kyle Hoffmann, and Dr. Matt Kade. These colleagues have taught me many things, and I will always be grateful for their help.

During my career, I spend three months at Sandia National Labs as a visiting researcher working with Geoff Brennecka, Gary Grest, and Matthew Lane. I will always remember the

amount of lab details I learned with Geoff when working with his group. Working with Gary and Matthew allowed me to obtain my first published paper, however, the most valuable part of this experience was learning how to do research from some of the greats in polymer science and materials science. During the four months with Tokyo Electron America, I worked with Ben Rathsack and Mark Somervell closely. I want to thank them for their help and discussions during my time there.

My PhD work has been graciously supported by This work is supported by the National Science Foundation through the Nanoscale Science and Engineering Center at the University of Wisconsin under Grant DMR-0832760, by the Semiconductor Research Corporation, and the use of the RedSky supercomputer for simulation time, Office of Naval Research for financial support of Multi-University Research Initiative (MURI Award N00014-11-1-0690), U.S. Department of Energy, Office of Science, Basic Energy Sciences, Materials Science and Engineering Division. An award of computer time was provided by the INCITE program of the Argonne Leadership Computing Facility,

I would have never been able to attend undergraduate or graduate school if it weren't for my parents, Randy and Cindy Peters. They have been a constant in my life and have supported my decisions in life. The value my parents put into education and work ethic has made me into the person I am today. My sister, BreeAnn Peters, deserves a special mention as someone I can count on in my life during the thick and thin. Jennifer Stinich deserves a special mention in this section because she will be joining my family soon, and she has the most to bear due to dealing with me on a daily basis.

ABSTRACT

Block copolymers have emerged as a compelling candidate for nanoscale fabrication. In the context of lithographic fabrication, attention has focused on the ability to control the self-assembly and orientation of the nanodomains. However, assembling the block copolymers into defect-free structures can be difficult. We know defect-free structures have a low free-energy in equilibrium, but defects still occur in experiments. This shows that the defects are occurring due to the kinetics and dynamics of the block copolymers. In this thesis, I explore two methods to reduce defects via the Hole-Shrink experiments and shear, and the first steps of a dynamic model to reduce defects in chemoepitaxy was developed. In the second chapter, the graphoepitaxial assembly of cylinder-forming block copolymers assembled into holes is investigated through theoretically informed coarse grained Monte Carlo simulations (TICG MC). The aim is to identify conditions leading to assembly of cylinders that span the entire thickness of the holes, thereby enabling applications in lithography. Three hole geometries are considered, including cylinders, elliptical cylinders, and capsule-shaped holes. Four distinct morphologies of cylinder forming poly(styrene-b-methyl methacrylate) (PS-b-PMMA) block copolymers are observed in cylinders and elliptical holes, including cylinders, spheres, partial cylinders, and wall-bound cylinders. Additional morphologies are observed in capsule shaped holes. PMMA cylinders that extend through the entire hole are found with PMMA-wetting surfaces; a weak wetting condition is needed on the bottom of the hole and a strong wetting condition is necessary on the sides of the hole. Simulated are also used to explore the morphologies that arise when holes are overfilled, or when PMMA homopolymers are added in blends with copolymers. We find that overfilling can alter considerably the morphological behavior of copolymers in cylinders and, for blends; we find that when the homopolymer concentration is ¿10%, the range of conditions for formation of PMMA cylinders that extend through the entire hole is increased. In general, results from simulations (TICG) are shown to be comparable to those of self-consistent (SCFT) calculations, except for conditions where fluctuations become important. In the third chapter, non-equilibrium

simulations of lamellae forming block copolymers are investigated by means of Theoretically Informed Coarse Grain Brownian dynamics simulations and Dissipative Particle Dynamics. Three lamellar orientations are subjected to steady shear, which differ in the direction of the microstructure with respect to the shear plane. The stable orientations are identified as a function of shear rate. It is found that for Brownian dynamics simulations the transition from parallel to perpendicular does not occur; however, by including local conservation of momentum, the lamellae exhibit this transition. The velocity profiles, stresses, and angles of the blocks in the system were analyzed to yield insights into why parallel orientations are less stable at higher shear rates.

In the fourth and fifth chapter, a model is developed for polymer entanglements in homopolymers and block copolymers. One possible approach relies on using slip springs. However, to inform these coarse grained models of block copolymers, the entanglements should be elucidated. Experiments do not provide the molecular data, so microscopic models are useful tools to study the molecular data. In this work, we study such issue using a Kremer-Grest model as it represents a ”microscopic model”. This model can be used to obtain the topological constraints of the polymer to inform coarse grained simulations. Defect annihilation of block copolymer nanodomains have been studied recently, and these studies have shown that there is a large kinetic barrier for defect annihilation. These studies has been performed with soft unentangled block copolymers, but in the experimental system, these block copolymers may be entangled. The entanglement effects of block copolymers are studied here using a slip spring model, which was previously developed for homopolymer melts. In this article, a comparison between the soft, slip spring model and a Lennard-Jones polymer is performed. The Lennard-Jones polymer is examined using the Z1 analysis, where it is shown that the topological constraints are increased at the interface of the unlike blocks for shorter chains, but for longer chains the constraints decrease at the interface. For the slip spring model, there is always a decrease of slip springs at the interface; when comparing the two models, we observe that large molecular soft chains mimic the Lennard-Jones polymers in both the topological constraints, but not the orientation of the chains near the interface.

CHAPTER 1

INTRODUCTION

Block copolymers are macromolecules which consist of two distinct polymer blocks connected by a covalent bond. These block copolymers exhibit microphase separation into structures on the order of 10 to 100 nanometers[3]. These macromolecules separate due to entropic (volume fractions) and enthalpic (chemical incompatibility) interactions, where the chemical incompatibility is characterized by the Flory-Huggins parameter χ, and the microphase separation is characterized by the degree of polymerization (N) and the volume fraction (f)[4]. In general, when the block copolymers phase separate into ordered microstructures of spheres, cylinders, bicontinuous or lamellar structures, they are composed of molten and solid states[4], with periodic microdomains of size 5 to 100 nm. This is called microphase separation. If there was not a covalent bond between the polymer blocks, the polymers would macrophase separate [5], similar to the separation between oil and vinegar. The chemical incompatibility of the block is enhanced with decreasing the temperature. At equilibrium, diblock copolymers exhibit three major morphologies, namely lamellae, hexagonally packed cylinders, and spheres in a body centered-cubic lattice. These self-assembled structures may be globally ordered by shear flow [6–12], chemical patterns [13–16], graphoepitaxy, and solvent annealing [17, 18].

When modeling block copolymers, the challenge is to accurately sum the competing terms of the interaction energy and the chain stretching entropy. Early theoretical work modeling block copolymers has been done by Self-Consistent Field Theory (SCFT), which models the block copolymer as a Gaussian chain[19–21]. Particle based models such as the Kremer-Grest model[22], TICG model[16, 23–29], and DPD models[30–32] have been extended to block copolymers to accurately predict the equilibrium and non-equilibrium properties. Block copolymers have emerged as a compelling candidate for nanoscale fabrication. The self-assembly of block copolymers can be directed by surface patterns, thereby creating templates for synthesis of organic and inorganic structures such as nanowires [33–35], quantum dots [36, 37], magnetic storage media [38], and silicon capacitors [39]. In the context of lithographic fabrication, attention has focused on the ability to control the self-assembly and orientation of the nanodomains [16]. However, assembling the block copolymers into defect-free structures can be difficult. We know defect-free structures have a low free-energy in equilibrium[40], but defects still occur in experiments[41]. This shows that the defects are occurring due to the kinetics and dynamics of the block copolymers[42, 43]. Recently, Hur *et al.* [44] showed that there are large kinetic barriers for direct self assembly, and chemical patterns reduce this kinetic barrier.

In the Hole-shrink simulations, the block polymer is used to reduce the lateral dimensions of the hole, and the question that arises is under which conditions will perfect cylinders be formed. I use simulations to identify the conditions that lead to perfect cylinder formation in so-called "contact-hole graphoepitaxy or Hole-shrink". The aim is to control the assembly of a block copolymer under cylindrical confinement, leading to formation of cylindrical morphologies that span the entire height of the domain. The material in the inner cylinder can then be removed selectively, thereby shrinking the original cavity or hole by as much as a factor of four [45]. Several recent reports have explored the morphologies that arise for a variety of materials[45–50]. Most studies, however, have only reported top-down SEM images of the resulting morphologies, and the precise three-dimensional nature of the assembly is not known.

The model is extended to Brownian dynamics and the Dissipative Particle Dynamics thermostat to examine its behavior under non-equilibrium molecular conditions, namely shear flow, using Lees-Edwards Boundary Conditions [51]. We examine the differences that arise when conservation of local momentum is enforced through DPD thermostats, and when Brownian dynamics approaches are employed.

The chains inside the nanodomains the specific blocks can become entangled. The entanglement effects on chain dynamics has been studied both theoretically [22, 23] and experimentally[52, 53]. These topological constraints hinder the self assembly of block copolymers for nanoscale fabrication[42]. Coarse grained soft polymer models are one way to explore these issues due to the ability to simulate long times and large length scales. However, models have not yet been developed to study the kinetics and dynamics of directed self assembly for large molecular weight block copolymers[54].

Here, I implement a particle-based, mean-field-theory-influenced block copolymer model to examine unentangled and entangled lamellae forming block copolymers equilibrium and in holes in a substrate (so-called Hole-Shrink experiments). I use Brownian dynamics, the Dissipative Particle Dynamics thermostat, and Monte Carlo simulations to solve the particle-based model. In the Hole-Shrink simulations, I compare my results to the Self-Consistent Field Theory of block copolymers (Chapter 1), and to examine the block copolymers in equilibrium, I use the Kremer-Grest model[55] as a base line (Chapter 3). The main objectives of this thesis are to understand the fundamentals of the Hole-Shrink process, the development of a state-of-the-art model for the dynamics of multi-chain simulations of homopolymers and block copolymers, and extending the state-of-the-art model of entangled homopolymers to block copolymers.

CHAPTER 2

GRAPHOEPITAXIAL ASSEMBLY OF CYLINDER FORMING BLOCK COPOLYMERS IN CYLINDRICAL HOLES.

The graphoepitaxial assembly of cylinder-forming block copolymers assembled into holes is investigated through theoretically informed coarse grained Monte Carlo simulations (TICG MC) and self-consistent field theory calculations (SCFT). The aim is to identify conditions leading to assembly of cylinders that span the entire thickness of the holes, thereby enabling applications in lithography. Three major hole geometries are considered, including cylinders, elliptical cylinders, and capsule-shaped holes. Four distinct morphologies of cylinder forming poly(styrene-*b*-methyl-methacrylate) (PS-*b*-PMMA) block copolymers are observed in cylinders and elliptical holes (cylinders, spheres, partial cylinders, and wall-bound cylinders). Many different morphologies are observed in capsule-shaped holes. PMMA cylinders that extend through the entire hole are found with PMMA-wetting surfaces; a weak wetting condition is needed on the bottom of the hole and a strong wetting condition is necessary on the sides of the hole. Overfilled holes are also simulated to explore the different morphologies that arise between the ideal cylindrical case and the overfilled case. PMMA homopolymers were also added in blends with copolymers under cylindrical confinement; when the homopolymer concentration is larger than 10%, the range of conditions for formation of PMMA cylinders that extend through the entire hole is increased. In general, it is found that results of simulations (TICG) and theoretical (SCFT) calculations are consistent with each other, which is discussed in the supplementary information. However, the SCFT calculations are less sensitive to surface interactions than MC simulations for the conditions explored in this work.

Copyright Statement

The material included in this chapter has been published in Journal of Polymer Science Part B: Polymer Physics. The full reference is: Brandon L Peters, Ben Rathsack, Mark Somervell, Takeo Nakano, Gerard Schmid, Juan J de Pablo "Graphoepitaxial assembly of cylinder forming block copolymers in cylindrical holes," *Journal of Polymer Science Part B: Polymer Physics* **53** (6), 430–441 (2015).

2.1 Introduction

The ability of block copolymers to assemble into ordered morphologies has been studied extensively, both in the bulk[3, 4] and in thin films[33–37]. For a variety of applications, it is of interest to generate defect-free ordered structures; this can be achieved through graphoepitaxy,chemical epitaxy[13–16, 56], and posts[57, 58]. In the area of semiconductor device manufacturing, recent efforts have focused on the use of block polymers in hole shrinking processes, in which thin interconnects are created by filling a relatively wide hole with a cylinder-forming polymeric material, whose characteristic dimensions are considerably smaller than those of the confining hole. The material in the inner cylinder can then be removed selectively, thereby shrinking the original cavity or hole by as much as a factor of four [45]. In design of so-called "hole-shrinking" or "contact-hole graphoepitaxy" processes, the central question thus becomes identifying the conditions leading to formation of ideal cylinders that span the entire thickness of the confining hole. In this work, we use simulations to identify such conditions.

Graphoepitaxy relies on topography to guide the assembly of block copolymers. This technique was developed over the last decade by several research groups. Segalman et al. [59–62] used primarily poly(styrene-*b*-2vinyl pyridine) (PS-*b*-P2VP) sphere forming block copolymers. Work by Cheng *et al.*[63, 64] also considered poly(styrene-*b*-ferrocenylsilane) (PS-*b*-PFS) sphere-forming diblock copolymers. One important outcome of that work was to show that defects in the confining walls can have a pronounced influence in the resulting morphology, and give rise to defective micro-domains[65].

Lamellar-forming poly(styrene-*b*-(ethyl-alt-propylene) (PS-*b*-PEP) block copolymers were also assembled in trenches under preferential wetting of the PS [66, 67]. Monolayers of horizontally oriented cylinders were assembled by Hammond *et al.* [68] using PS-*b*-P2VP over a PS wetting substrate. Good assembly was observed in trenches of up to three micrometers[69]. More recently, the assembly of vertically oriented cylinders of poly(styrene-*b*-methyl methacrylate) (PS-*b*-PMMA) by graphoepitaxy has been explored in several papers [45–50]. Vertically aligned cylinders are found to behave similarly to PS-*b*-PFS spheres, where the width and height of the trenches control the orientation, and where a neutral wall gives rise to the best assembly. Most experimental studies to date, however, have only reported top-down SEM images of the resulting morphologies, and the precise three-dimensional nature of the assembly is not known.

Directed assembly with inhomogeneous walls can also enable alignment of lamellae forming block copolymers of PS-*b*-PMMA[70]. In particular, a neutral bottom surface and a preferential side-wall interaction are known to produce vertically oriented domains. A similar approach was used to investigate the assembly of block copolymers in cylindrical pores by Shin et al.[71].

Theoretical and computational studies of graphoepitaxial assembly of block copolymers have generally relied in self-consistent field theory (SCFT) and Monte Carlo simulations. Past studies considered lamellae-forming [20, 72] and cylinder-forming materials[73, 74, 74–76]. In this work, we present a systematic computational study of the morphologies that arise in hole-shrinking applications. We consider the particular case of cylinder-forming PS-*b*-PMMA block copolymers, and we examine the effect of the confinement geometry and wetting characteristics on assembly. It is found that cylinder formation through the entire hole is difficult in perfect cylindrical geometries; however, when the holes are slightly deformed, the range of parameters for the formation of full cylinders is increased. Extending the lateral dimensions beyond ellipses to capsule-shaped geometries produces “U” and “W” shaped morphologies. Addition of homopolymers improves the assembly process, and overfilling of the holes can under some circumstances also lead to a PMMA cylinders that extend through the entire hole.

2.2 Model and Methods

2.2.1 Monte Carlo

The model used for the block copolymers was the model developed by Helfand [77], which includes the chain connectivity, incompatibility of the polymer blocks, and the compressibility. The chains are Gaussian in nature which are discretized into N beads connected by springs. The bonded Hamiltonian can be written as the following,

$$\frac{H_b(r_i(s))}{k_B T} = \frac{3}{2} \sum_{i<j} \left(\frac{r_{ij}}{b}\right)^2 B_{ij} \tag{2.1}$$

where the position of the s^{th} bead on the i^{th} chain is $\mathbf{r_i}(\mathbf{s})$, the sum runs over all beads (Nn) (where n is the number of chains), B_{ij} is either unity if there is a bond linking the beads or zero otherwise, $b^2 = R_e^2/(N-1)$, R_e is the average end to end distance of the polymer chains. The non-bonded interactions includes the Flory-Huggins parameter (χN), which controls the incompatibility between monomers and the compressibility (κN), where non-bonded Hamiltonian is the following equation,

$$\frac{H_{nb}[\phi_A, \phi_B]}{k_B T} = \sqrt{\mathcal{N}} \int_V \frac{dr}{R_e^3} [\chi N \phi_A \phi_B + \frac{\kappa N}{2}(1 - \phi_A - \phi_B)^2] \tag{2.2}$$

k_B is the Boltzmann constant, n is the number of chains, ϕ_K is the normalized local densities of type A or B beads, ρ_0 is the normalized density, and $\sqrt{\mathcal{N}} = \rho_0 R_e^3/N$ is the number of chains per unit chain volume, which can be extracted from experiments. In cases where there is an interaction between the substrate and the polymer, *e.g*, graphoeptiaxial assembly of block copolymers, the following substrate potential is given by,

$$\frac{U_S\left(\mathbf{r},K\right)}{k_BT}=f(x,y,K)\frac{\Lambda^K}{d_s}\exp\frac{-z^2}{2d_s^2}\quad. \tag{2.3}$$

where, z is the distance normal to the surface, and d_s is the decay length of the potential. The strength of the interaction is controlled by $\Lambda^K N$, and K is either a monomer of type A or B; the parameter is found from comparing the surface free energies of the components[78]. The function $f(x,y,K)$ has an absolute value of one, and it can change the sign depending on K and x,y. For example, if a bead of type B is in a position where a chemical pattern is preferential to A, then the sign of $f(x,y,K)$ is positive, and $\Lambda^A=-\Lambda^B$. Thus the surface contribution to the energy is

$$H_S(\mathbf{r},K)=\sum_{i=1}^{nN}U_S\left(\mathbf{r},K\right). \tag{2.4}$$

The total Hamiltonian is given by the sum of all the components:

$$H(\mathbf{r}_i(s))=H_b(\mathbf{r}_i(s))+H_{nb}[\phi_A,\phi_B]+H_S(\mathbf{r},K). \tag{2.5}$$

This model has been widely used in bulk studies of copolymers[25, 79], for polymer dynamics[24, 80], and for thin films[16, 26–29, 56, 81, 82]. In our own work the model is implemented in Monte Carlo or Langevin dynamics simulations. In Monte Carlo simulations, each bead is randomly displaced, on average, once every Monte Carlo step; the trial positions of the bead's or group of bead's are accepted with probability $p_{acc}=min[1,exp\frac{-\Delta U}{k_BT}]$, where ΔU is the change in the non-bonded, substrate, and bonded potential energies for the trial move. Representative Monte Carlo moves include single displacements, translations, switch moves, and reptation moves; additional details can be found in Detchevery *et al.* [26] and Baschnagel *et al.* [83]. The simulations presented here are carried out in the NVT ensemble, and a grid based method is used to calculate the local energies[26].

2.2.2 Self-Consisten Field Theory

The self-consistent field theory (SCFT) simulations were performed with the model as described by Matsen[19, 20]. However, the saddle point field equations were solved via an Euler update scheme, while the diffusion equation was solved with a pseudo-spectral method [21]. The SCFT simulations were three dimensional, with sine basis functions used for the boundary conditions, as described by Hur, *et al*[73]. The wall potential was the same function used as in the Monte Carlo simulations, as opposed to the wall potential used by Matsen[20]. The total free energy of the system is given as follows

$$\begin{aligned}
&\tfrac{F[\phi_A,\omega_A,\phi_B,\omega_B,\phi_B,\xi]}{nk_BT} \equiv -\ln Q[\omega_A,\omega_B] \\
&+V^{-1}\int dr[\chi N\phi_A(\mathbf{r})\phi_B(\mathbf{r})- \\
&U_S N(\phi_A(\mathbf{r})-\phi_{\mathbf{B}}(\mathbf{r}))-\omega_{\mathbf{A}}(\mathbf{r})\phi_{\mathbf{A}}(\mathbf{r})-\omega_{\mathbf{B}}(\mathbf{r})\phi_{\mathbf{B}}(\mathbf{r})- \\
&\xi(\mathbf{r})(\phi_{\mathbf{0}}(\mathbf{r})-\phi_{\mathbf{A}}(\mathbf{r})-\phi_{\mathbf{B}}(\mathbf{r}))]
\end{aligned} \tag{2.6}$$

where

$$Q[\omega_A,\omega_B] \equiv \int drP[\mathbf{r}_\alpha;0,1]\exp\left[\int_0^f ds\omega_A(\mathbf{r}_\alpha(\mathbf{s}))-\int_f^1 ds\omega_B(\mathbf{r}_\alpha(\mathbf{s}))\right] \tag{2.7}$$

Q is the partition function of a polymer in external fields ω_A and ω_B, $\xi(\mathbf{r})$ Lagrange-multiplier field, P is the probability of a Gaussian chain, f is the fraction of the A block, ϕ_0 is the total density of the system, and ϕ_A and ϕ_B are the monomer densities. Additional definitions for these variables are given by Matsen[20].

2.2.3 Parameters

Our simulations consider a 24K-b-47K poly(methyl methacrylate)-b-polystyrene block copolymer[45, 46]. This corresponds to $\sqrt{\mathcal{N}}=116$, $\chi N_{MC}=26$, $\chi N_{SCFT}=21.32$[25], $d_s=0.15$ and

$\kappa N = 35$. We choose $N = 33$ for the Monte Carlo simulations, but for both methods, $f = 0.33$. The natural periodicity $L_0 = 1.78$ for MC and 1.55 for SCFT.

2.3 Results

2.3.1 Monte Carlo Simulations

The first geometry considered here consists of a cylindrical hole, similar to that used in the experiments by Yi *et al.* and Seino *et al.* [45, 46]. Specifically, the radius (r_c) is set to 40 nm, and the height (L_z) of the hole is set to 60 nm. The interaction between the substrate and PMMA (block A) on the sides of the cylinder is denoted by Λ_s, and the interaction between the bottom of the cylindrical hole and PMMA is denoted by Λ_b. The top surface of the cylindrical hole is considered to be neutral to PMMA and PS. In this article, we have only explored the PMMA wetting condition because it produces smaller PMMA cylinders[84, 85].

We begin by focusing on a ratio of the diameter (D) to the natural periodicity (L_0) of $D/L_0 = 2$, which in experiments corresponds to the optimal conditions for the formation o PMMA cylinders[45]. The simulation is set up as seen in Figure 2.1a. The values of Λ_b and Λ_s are varied from 0.2 to 2.2, and results are shown in Figure 2.2c. At low values of Λ_b and all values of Λ_s, PMMA cylinders that extend through the entire hole are observed (Figure 2.2a), which will be referred to as "full" cylinders. For higher values, only partial PMMA cylinders are formed (Figure 2.2b), which we referred to as "partial" cylinders. As the value of D/L_0 increases, full cylinders appear in a smaller range of parameters, as can be seen in Figures 2.2d-f. The height of the hole (L_z and Figure 2.1c) is also an important variable. The images in Figure 2.3a and b show an increase in the range of parameters leading to full cylinders when the height is increased by 0.4 R_e (18 nm) at the larger values of $D/L_0 = 2.28$ or 2.44.

Experiments have used a wet-development process to remove the PMMA from the hole; from this information, it is believed that the PMMA cylinders do not extend through the entire hole. According to Seino *et al.*[45], some PS remains at the bottom after the wet-development process. If the partial cylinders were etched as in Seino *et al.*'s experiments[45], PS at the bottom of the hole would interfere with the subsequent lithographic steps and pattern transfer. Our findings are consistent with these observations, if we consider that the upper right of the phase diagram in Figure 2.2c corresponds to the polymer/wall interactions used in past experiments.

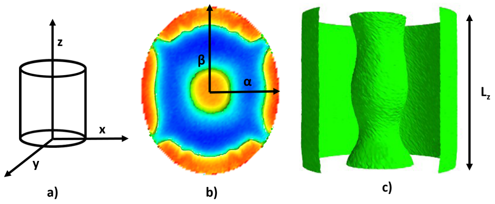

Figure 2.1: Image a) shows the set up of the cylindrical hole, b) shows the minor (α) and major axis(β) of the cylindrical or elliptical hole, and c) shows the height of the film (L_z) and an example morphology of a PMMA cylinder that extends through the entire hole. In image b), the red is PMMA and the blue is PS, and the green is the interface between block A and B($\Phi = \frac{\phi_A - \phi_B}{\phi_A + \phi_B} = 0$) in images b) and c).

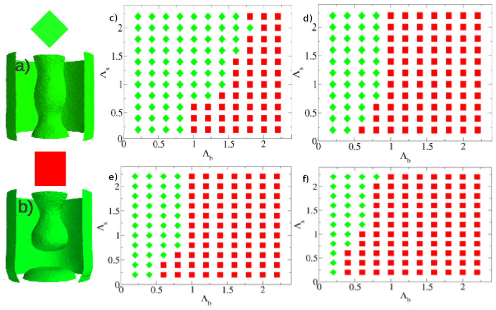

Figure 2.2: Image a) is an example morphology of a cylinder that extends through the entire hole, and image b) is an example morphology of a partial cylinder. The green is the interface between block A and B($\Phi = \frac{\phi_A - \phi_B}{\phi_A + \phi_B} = 0$). Morphologies observed for a PS-*b*-PMMA cylinder forming block copolymer with the height of the hole of 60 nm and values of c)D/L_0=2.0 d) D/L_0=2.12 e) D/L_0=2.28 f)D/L_0=2.44. Red squares are partial cylinders.

Eventually, however, the range of parameters for full cylinders becomes small (see Figure 2.4a) when D/L_0 deviates significantly from 2 (see, for example, results for $D/L_0 = 2.61$). Overall, we find that three morphologies can appear as the strength of the interactions is varied: full cylinders, partial cylinders, and spheres (Figure 2.4e). To obtain a full cylinder,

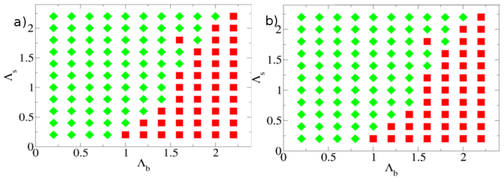

Figure 2.3: Morphologies observed for a PS-b-PMMA cylinder forming block copolymer with the height of the hole of 78 nm and values of a) D/L_0=2.28b) D/L_0=2.44. Red squares are partial cylinders (Figure 2.2b) and green diamonds are full cylinders (Figure 2.2a).

Λ_b must be weak and Λ_s must be strong; partial cylinders are formed with a large value of Λ_b and Λ_s. At low to moderate values of Λ_s, spherical morphologies are observed. Full cylinders occur when the interaction with the side wall is strong because there is a larger density of chains near the side wall and, therefore, less PMMA in the middle of the hole. This combination of interactions mimics the effect of lower values of D/L_0. With lower values of the wall/polymer interaction and larger values of D/L_0, the PMMA block wants to form a doughnut shape consisting of a cylinder that connects with itself; however, the diameter of the cylindrical hole is not large enough to permit formation of a full doughnut, so a sphere is formed in its place. When the strength of the wall/polymer interaction increases at the bottom and the side of the hole there is not enough PMMA in the middle of the hole to form a full cylinder, therefore, partial cylinders appear instead (which correspond to the upper right-hand corner of the phase diagrams). The smallest concentration of PMMA in the middle of the hole forms partial cylinders, and as the concentration increases, full cylinders are formed; finally, the largest amount of PMMA is the sphere morphology because the polymer wants to form a doughnut, as mentioned before.

It is also of interest to consider assembly in elliptical cylinders; as discussed below, such deformations can change the block copolymer morphology and lead to desirable results. Parameters α (minor axis) and β (major axis) (Figure 2.1) describe the shape of an ellipse according to ($\frac{x^2}{\alpha^2} + \frac{y^2}{\beta^2} = 1$). Here we consider $1\%, 5\%$, and 10% deformations from an ideal cylinder. The 10% deformation corresponds to $\alpha = 0.90 r_c$ and $\beta = 1.1111 r_c$; note that a constant volume is maintained for all deformations when comparing to the original cylindrical hole. In the remainder of this section, the deformations considered here are denoted as E99 for 1%, E95 for 5%, and E90 for 10%. Figures 2.5b-d show several representative configurations. A value of D/L_0=2.63 was chosen due to the fact that the number of full cylinders in the phase diagram were small. Four morphologies are observed in elliptical holes: partial cylinders, full cylinders, spheres, and wall-bound cylinders (Figure 2.4f). The three elliptical geometries exhibit the same general trends described earlier for ideal cylindrical holes. However, in addition to the spherical morphologies, wall-bound cylinders are also observed. The range of parameters where partial cylinders exist in the phase diagram increases for all three elliptical geometries; however, the range of parameters for full cylinder formation is slightly increased in the E90 case. The resulting morphologies are shown in Figure 2.6. Less PMMA wets the walls, allowing for the full cylinder to be formed. As the walls are deformed, some of the PMMA chains are stretched; for the E90 case, the chains have an end-to-end distance of $0.38R_e$ on a section of the walls (section b in Figure 2.7), which is larger than the bulk value of $0.33R_e$. The stretching of the chains occurs near the ellipse surface, due to the smaller curvature of the minor axis. PMMA chains have a bulk-like end-to-end distance at the surface of the major axis (Section a of Figure 2.7) due to the higher curvature of the walls. The bulk-like allow more PS to approach the walls at lower values of Λ_s because the PMMA chains are taking up less volume near the walls. This can be seen in the top down image in Figure 2.7. The PMMA full cylinder can now be formed because the same amount of PMMA can be located in the center of the hole as in the cases with lower D/L_0 values. When Λ_b increases and a low value of Λ_s is maintained, the PMMA creates cylinders around the edges which connect to the middle PMMA cylinder, where the morphologies are no longer distinct.

Yi *et al.*[46, 47] observed multiple cylinders when the holes were elongated; to address these observations, here we use two semi-circles attached to a rectangle to create what we call a "capsule-shaped" geometry. The longest length is L_y and the height of the rectangle is a; a representative configuration is provided in Figure 2.5e. We use $L_y = 2r_m + a$ to examine

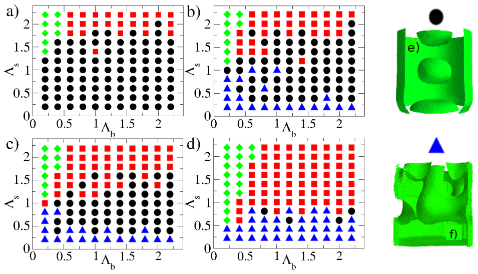

Figure 2.4: Morphologies observed for a PS-b-PMMA cylinder forming block copolymer with the geometries a) C and $D/L_0 = 2.61$, b) E99, c) E95, d) E90. Black circles are spheres (image e), red squares are partial cylinders (Figure 2.2b), green diamonds are full cylinders (Figure 2.2a), and blue triangles are wall-bound cylinders (image f). The green in image e) and f) is the interface between block A and B($\Phi = \frac{\phi_A - \phi_B}{\phi_A + \phi_B} = 0$). The value of D/L_0 is 2.61 for the cylindrical hole.

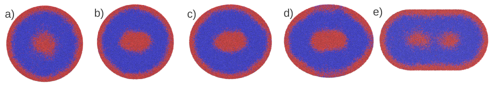

Figure 2.5: Snap shots of top down views for a) C, b) E99, c) E95, d) E90, e) Capsule-shape. Red is PMMA and Blue is PS.

how the morphology changes as a is increased, where $r_m = 30nm$ is the radius of the semicircles; a value $L_z = 50nm$ is used for the depth of the hole. In Figure 2.8, the morphologies start from a single partial cylinder and end with a “U” shaped PMMA domain. The latter domains are fairly stable; however, they do change in size ($\Lambda_s = 1.4$ and $\Lambda_b = 0.8$), as a increases. The U-shape morphology dominates the phase diagram, largely because there is more space in the middle of the domain for this morphology to form. Figures 2.8e and f show that, for values above $\Lambda_b = 1.6$ and below $\Lambda_s = 0.2$, one can even form an “H”-shape domain.

The morphologies that extend to the bottom of the surface do not correspond to two distinct cylinders; the two domains are always connected, as can be seen in Figure 2.9 e and f. When a is increased, wall-connecting cylinders do appear, but when the capsule-shaped geometry shows two circles on the top-down image, wall-bound cylinders do not appear. When the holes are elongated even further, we see the formation of a different morphology. As seen in Figures 2.9e-g, one section of the U-shape becomes larger and eventually breaks

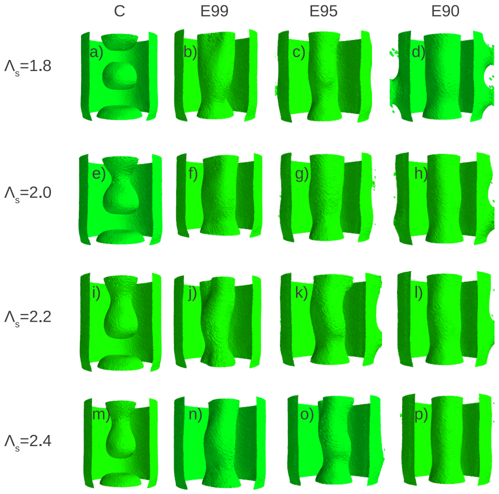

Figure 2.6: Comparison of interface between block A and block B ($\Phi = \frac{\phi_A - \phi_B}{\phi_A + \phi_B} = 0$) C, E99, E95, E90. All images have $\Lambda_b = 0.4$ and Λ_s range from 1.6 to 2.2. A slice of the interface near the wall is removed for clarity. Figures were generated using an Open-Source Scientific Visualization Software, Mayavi2[1]. The value of D/L_0 is 2.61 for the cylindrical hole.

into a W-shape.

Recent experiments have also shown that, after annealing, the prepatterns are not perfectly filled by the block copolymers, and that overfilling is common. To examine the consequences of overfilling, we used a periodic box in x and y above the cylindrical hole. A hard top surface is used in the z direction instead of a free surface due to the fact that the MC model used here is a space filling model. The strength of the wall/polymer interaction above the hole is the same as in the bottom of the hole, and the values of the wall/polymer interaction were varied from 0.2 to 2.2 as before. A few values of the wall/polymer interactions were selected to illustrate important trends and morphologies, as seen in Figure 2.10. The images in Figures 2.10a-c correspond to the full cylinder, sphere, and partial cylinder cases, respectively, investigated in the cylindrical hole earlier. Overfilling leads to morphologies that exhibit a different trend to that observed earlier. Full cylinders are seen when Λ_s is large and Λ_b small, and when Λ_s and Λ_b are large, spheres appear (Figure 2.10c). At intermediate strengths of the wall/polymer interaction, morphologies similar to those in Figure 2.10b are observed. With overfilling, the interaction of the PMMA with the wall above the hole (and more PS outside of the hole) leads to a different phase diagram. As can be seen

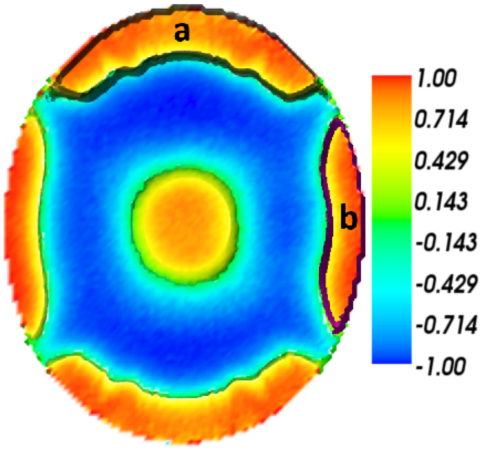

Figure 2.7: Image of a top down view of E90 with a $\Lambda_b = 0.2$ and $\Lambda_s = 2.2$, to show the areas with different end-to-end distances in the wetting layer. Section a has an end-to-end distance of $0.33R_e$, while section b has an end-to-end distance of $0.38R_e$. The legend plots $\Phi = \frac{\phi_A - \phi_B}{\phi_A + \phi_B}$, where A is PMMA and B is PS.

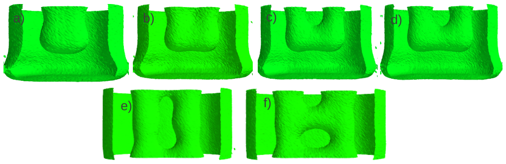

Figure 2.8: Comparison of interface between block A and block B ($\Phi = \frac{\phi_A - \phi_B}{\phi_A + \phi_B} = 0$) for increasing $L_y = 2r_m + a$ to show the transition between one and two holes. a) $L_y = 2r_m + a = 80.92nm$, b) $L_y = 89.62nm$, c) $L_y = 98.32nm$, d) $L_y = 107.02nm$, e)$L_y = 106.98nm$, and f)$L_y = 115.68nm$. Images a-d have $\Lambda_s = 1.4$ and $\Lambda_b = 0.8$, and images e and f have $\Lambda_s = 0.2$ and $\Lambda_b = 1.6$. A slice of the interface near the wall is removed for clarity Figures were generated using an Open-Source Scientific Visualization Software, Mayavi2[1].

in the Figure, when the PS diffuses out of the hole, it creates a layer of PMMA at the top of the hole at higher wall/polymer strengths.

It is well known that homopolymers can be used to alter domain spacing. Figure 2.11 shows the phase diagram that arises when different amounts of PMMA homopolymer are added to the system in a cylindrical hole. The homopolymers have a chain length of $N = 12$. The homopolymers were described according to details provided in Stoykovich *et al*[13]. hWen the homopolymer concentration is 5%, there are fewer full cylinders and more partial cylinders. The phase boundaries between partial cylinders and spheres are not as well

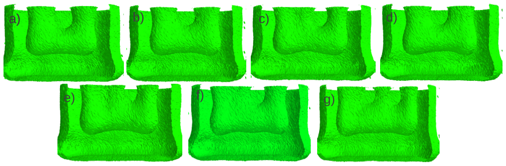

Figure 2.9: Comparison of interface between block A and block B ($\Phi = \frac{\phi_A - \phi_B}{\phi_A + \phi_B} = 0$) for increasing L_y to show the transition between two and three cylinders. a) $L_y = 2r_m + a = 108.76nm$, b) $L_y = 110.50nm$, c) $L_y = 112.24nm$, d) $L_y = 113.98nm$ e) $L_y = 115.72nm$ where, f) $L_y = 124.42nm$, and g) $L_y = 133.12nm$. All images have $\Lambda_s = 1.4$ and $\Lambda_b = 0.8$. A slice of the interface near the wall is removed for clarity. Figures were generated using an Open-Source Scientific Visualization Software, Mayavi2[1].

defined as in 2.4a. For 10% and 20% homopolymers, the range of parameters for partial cylinders increases; however, with 20% homopolymers, the range of parameters for full cylinders also increases. The homopolymers are equally spread through the PMMA domains. If one compares the images from the pure block copolymer case and the binary blend, the morphologies are quite different. The homopolymer swells the morphology in the middle of the hole (homopolymers relieve the stress in the system), and at the specific diameter studied here, different structures are formed because there is less PS in the hole.

Lastly, we also examined the critical dimensions and deformation of the PMMA domains. The radius of the PMMA domain in experiments by Seino *et al.* [45] was between 20 and 22 nm; however, our simulations of the cylindrical hole yield an average radius of 25 nm for a partial cylinder. The difference between the experiments and the simulations is small, but could be due to the precise nature of the wetting conditions (which are not precisely known in experiments), and to small deviations from a perfectly cylindrical hole geometry. In Yi, *et al.*[47], the deviation of the PMMA domains (how much the PMMA cylinders deviate from the average placement) of the capsule-shaped hole was calculated, and the authors found that there is more deviation in the larger direction. In the simulations, the same calculations were performed with partial cylinders for 31 different seeds, but only the top 10% of the PMMA hole. The center of mass of the PMMA blocks were tracked throughout the simulation, and the standard deviation was evaluated through the probability that the center of mass of the chains be displaced away from the center of the hole (or from the center of the capsule-shaped geometry). For the cylindrical hole, the standard deviation was 0.1 nm in the x and y directions (geometry seen in 2.1). The capsule-shaped hole had a standard deviation of 0.12 nm and 0.18 nm for two PMMA domains, and of 0.13 nm and 0.2 nm for PMMA domains for the smaller and larger direction, respectively. While the values of the simulations are much smaller than the values reported in experiments, the same general trends are observed here. The discrepancies between the simulations and experimental values comes from the hole is not perfect in experiments (top down and through the substrate), non-perfect wetting conditions, imperfect etching, polydispersity, and the mesa wetting the PMMA block. These simulations have perfect conditions for each of these cases and no overfilling, showing that if one were able to alleviate all those issues the deviation would be minimal.

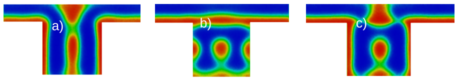

Figure 2.10: The images present cross sections of the center of the cylindrical hole and the box on top of the hole. Image a) has the polymer/wall interactions of of $\Lambda_s = 1.8$ and $\Lambda_b = 0.2$, b) has the polymer/wall interactions of $\Lambda_s = 0.2$ and $\Lambda_b = 0.6$, and c) has the polymer/wall interactions of $\Lambda_s = 1.6$ and $\Lambda_b = 1.0$. The cylindrical hole has a value of $D/L_0 = 2.61$

2.3.2 Self-Consistent Field Theory

We also explore the use of SCFT on the equivalent geometry and parameters as those used in MC simulations, except χN was rescaled as proposed in the literature[25]. For cases where the MC indicate formation of full cylinders (Figures 2.12d and e), SCFT (Figures 2.12a and b) exhibits a ring of PMMA around a PS cylinder (a donut shape). The difference remains when examining the partial cylinder. Contrary to the results of MC simulations, SCFT morphologies do not change as much as the MC simulations when Λ_s and Λ_b are varied.

The discrepancies between SCFT and MC results are two fold. First, a value of $\chi N_{SCFT} = 21.3$ was used; it is known that near the order-disorder transition SCFT model used here is

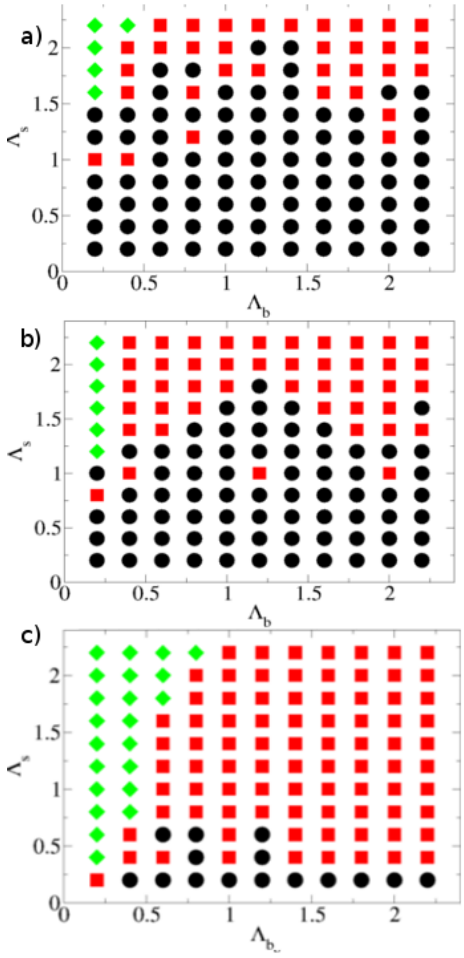

Figure 2.11: Morphologies observed for a) 5% homopolymers b) 10% homopolymers, and c)20% homopolymers. Black circles are spheres (Figure 2.4e), red squares are partial cylinders (Figure 2.2b), green diamonds are full cylinders (Figure 2.2a). These simulations are cylindrical holes with a value of D/L_0 is 2.61.

not correct. For large values of χN SCFT reproduces experimental data, but at the lower values of χN presented here, fluctuation effects become important. However, when the molecular weight of the block copolymer reaches infinity (no fluctuations), the SCFT and MC results will be the same. Since the MC results here are at an experimentally relevent density[25], the only difference between the models should be the fluctuations. Second, SCFT is known to be inaccurate near phase transitions. When the MC simulations show a phase transition while changing Λ_s and Λ_b, the SCFT results do not. In Figure 2.12, there are no partial cylinders and full cylinders for the diameter used in these simulations; however, if the diameter is reduced, the SCFT does show partial cylinders and full cylinders as well as in the MC simulations. The donut shape is seen in the MC simulations when the diameter of the hole is increased. It's hypothesized that the fluctuations in the MC model cause the donut structures in SCFT to collapse to the sphere; however, if the hole is large enough, the fluctuations aren't strong enough to collapse to the sphere. Lastly, there are major differences between the SCFT and MC when comparing the values of D/L_0. As the values of D/L_0 decreases, it can be seen that the SCFT simulations show a sphere or donut shape where the MC simulations show full cylinders. This difference is due to the fluctuations in the MC simulations stabilize the sphere to a full cylinder.

Finally, we note here that the computational time for an individual MC simulation run is approximately 24 hours on a single processor with 100,000 MC steps. An individual SCFT run requires 48 hours to observe a morphology and 96 hours to reliably converge to the minimum free energy to an residual of 10^8.

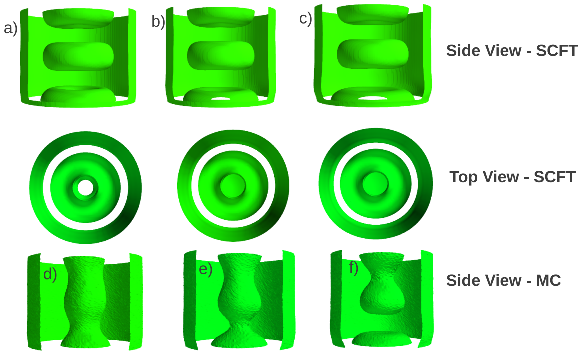

Figure 2.12: SCFT for a) $\Lambda_b = 0.2$, b) $\Lambda_b = 0.4$, c) $\Lambda_b = 0.6$. For all images, $\Lambda_s = 1.6$. These compare to MC images for the same Λ_b and Λ_s. Image a compares to d, image b compares to e, and image c compares to f. Figures were generated using an Open-Source Scientific Visualization Software, Mayavi2[1].

2.4 Conclusions

Monte Carlo simulations using the Theoretically Informed Coarse Grained (TICG) model have been used to explore the behavior of cylinder-forming copolymers confined in hole

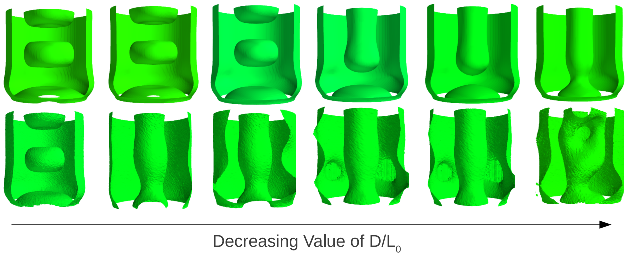

Figure 2.13: SCFT (top) and MC (bottom) images for different values of D/L_0. The images on the left are D/L_0=2.61 and on the right D/L_0=1.83. Figures were generated using an Open-Source Scientific Visualization Software, Mayavi2[1].

geometries. Specifically, we considered cylindrical holes, elliptical holes, and capsule-shaped geometries. For cylindrical holes, an increase of the height of the hole allows the system to form full cylinders at over a relatively wide range of surface-polymer interactions (low values of Λ_s and Λ_b). Near $D/L_0 = 2.0$ our results are consistent with available experiments for string interactions between the polymer and bottom and side walls of the holes. However as D/L_0 is increased, the morphology of the system is dominated by spheres. Partial cylinders appear for strong wall polymer interactions. By deforming the hole to an ellipse, it becomes possible to form full cylinders over a wider range of conditions than in perfectly cylindrical holes.

Deforming the cylinders into a capsule-shaped geometries, however, results in the PMMA cylinder becoming wider and eventually breaking into a U-shape morphology. The morphologies in the capsule-shaped geometry are relatively stable to elongation of the capsule-shaped geometry. At higher values of Λ_b and smaller values Λ_s, full cylinders can be formed; however, U-shape domains tend to dominate the phase diagram. As the length of the capsules increases, the U-shape evolves into a W-shape. The same trend discussed above for the U-shape can be seen in the W-shape. Addition of homopolymers, at concentrations in the vicinity of 20%, also increases the range of conditions over which full cylinders are observed.

Latypov, *et al.*[86] showed, using the Monte Carlo model in this work, provide similar results, however, at low values of PMMA volume fraction, an unstable morphology was observed. The article studed the optimization of the confinement hole for the DSA process, using SCFT. Iwama, *et al.*[87] used SCFT to examine critical dimensions, volume fractions, wetting conditions, and the effect of homopolymers on the assembly of the block copolymers in the confined holes. Further work by the same group[84, 88–92], explore cylindrical confinement in more detail using SCFT. The SCFT results are similar to the calculations showed in the supplementary information, as well as connecting cylinders in the capsule-shaped case. Fukawatase, *et al.*[93] used the Ohta-Kawasaki (OK) model for the hole shrink simulations, and showed reasonable accuracy when compared to SCFT. The results showed that with a neutral bottom surface, there was a defect-free window. We conclude this work by saying the past theoretical studies of copolymer morphology in cylinders have been carried out using SCFT/OK are largely consistent with the results presented here, except in regions were fluctuations are expected to be important. The results shown here illustrate that the fluctuations are important to understand the hole shrink problem.

CHAPTER 3

NON-EQUILIBRIUM SIMULATIONS OF LAMELLAE FORMING BLOCK COPOLYMERS UNDER STEADY SHEAR: A COMPARISON OF DISSIPATIVE PARTICLE DYNAMICS AND BROWNIAN DYNAMICS

Non-equilibrium simulations of lamellae forming block copolymers are investigated by means of Theoretically Informed Coarse Grain Brownian dynamics simulations and Dissipative Particle Dynamics. Three lamellar orientations are subjected to steady shear, which differ in the direction of the microstructure with respect to the shear plane. The stable orientations are identified as a function of shear rate. It is found that for Brownian dynamics simulations the transition from parallel to perpendicular does not occur; however, by including local conservation of momentum, the lamellae exhibit this transition. The velocity profiles, stresses, and angles of the blocks in the system were analyzed to yield insights into why parallel orientations are less stable at higher shear rates.

Copyright Statement

The material included in this chapter has been published in Macromolecules. Reprinted (adapted) with permission from: Brandon L Peters, Abelardo Ramrez-Hernndez, Darin Q Pike, Marcus Muller, Juan J de Pablo “Nonequilibrium simulations of lamellae forming block copolymers under steady shear: A comparison of dissipative particle dynamics and Brownian dynamics,” *Macromolecules* **19** (45), 8109–8116 (2012). Copyright (2015) American Chemical Society

3.1 Introduction

At equilibrium, diblock copolymers exhibit three major morphologies, namely lamellae, hexagonally packed cylinders, and spheres in a body centered-cubic lattice. These self-assembled structures may be globally ordered by shear flow [6–12], chemical patterns [13–16], graphoepitaxy, and solvent annealing [17, 18]. The lamellar structures and their response to steady shear flow are the focus of this paper. Figure 3.1 shows three distinct lamellar orientations that are subjected to shear; these are labeled parallel(‖), perpendicular(⊥), and transverse ($\mathcal{T}$), according to the normal of the lamellae with respect to the direction of the shear plane. The lamellae normals are parallel to the velocity gradient, the vorticity, and the flow direction, respectively.

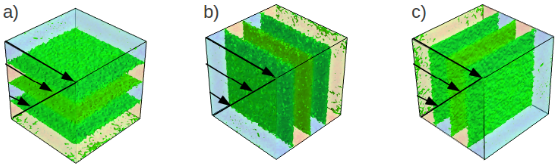

Figure 3.1: Schematic representation of lamellae: (a) parallel (‖), (b) perpendicular (⊥), and (c) transverse ($\mathcal{T}$) orientations. Figures were generated using an Open-Source Scientific Visualization Software, Mayavi2[1].

Depending on frequency and strain, the application of an oscillatory flow to copolymer melts or solutions just below the order-disorder transition (ODT) results in stable ‖ and ⊥ orientations. Initially, Koppi *et al.* [94, 95], found that the perpendicular morphology was obtained at high frequencies and elevated temperatures, and the parallel morphology was observed otherwise; their experiments were conducted on a poly(ethylene-propylene)-b-poly(ethyl ethylene) (PEE-b-PEP) block copolymer. The transition from the parallel morphology to the perpendicular morphology was also seen at higher frequencies, but the reverse was not found. For polystyrene-b-polyisoprene (PS-b-PI), Patel *et al.* [96] and Riise *et al.* [97] obtained the parallel orientation at high frequencies and the perpendicular orientation at low frequencies. Gupta *et al.* [98], showed that at high frequencies the parallel morphology is stable and at lower frequencies the perpendicular morphology is stable for a

PS-b-PI lamellae forming block copolymer. Leist *et al.* [99] found two transitions from $\| \rightarrow \perp \rightarrow \|$ as the oscillatory frequency was lowered. Leist *et al.* [99] showed that the shear rate can be mapped directly onto the oscillatory shear. The flip back to parallel at higher shear rates is in contradiction with the theoretical work of Fredrickson [100]; lack of a double flip in theory has been attributed to wall flow interactions in the experiments [101]. The reviews by Chen *et al.* [102], and Hamley [103] provide an extensive discussion of the morphologies observed in experiments. In general, the deformation of the block copolymer comes from large amplitude oscillatory shear (LAOS), where the oscillatory frequency governs the reorientation of the lamellar structures [7, 94–97].

Several theoretical studies have considered the effect of steady shear on lamellar forming block copolymers in the bulk [30–32, 100, 101]. Fredrickson [100] performed a study using a mean field theory block copolymer model with a simple stochastic model of the dynamics, and showed that near the ODT at low shear stress the parallel morphology is stable, and at higher shear stress the perpendicular morphology is stable. The study did not examine the actual transition between the parallel orientation and the perpendicular orientation. Rychkov [101] used non-equilibrium molecular dynamics using a Lennard-Jones (LJ) polymer model and SLLOD equations of motion for planar Couette shear flow, and found that sphere and cylinder forming block copolymers in solution change morphology to the parallel lamellar orientation at low shear rates and to the perpendicular lamellar orientation at higher shear rates. Cui *et al.* [104] used self-consistent field theory with the lattice Boltzmann method to find the stable orientations for a symmetric block copolymer. At low shear frequencies a parallel orientation was observed, and at higher frequencies a perpendicular morphology was seen. Note that their initial state was only a totally disordered state.

Guo *et al.* [30] studied lamellae-forming block copolymers using short chains of LJ particles with a dissipative particle dynamics (DPD) thermostat using the reverse non-equilibrium algorithm of Müller-Plathe (MP) to induce a shear velocity profile. The transitions from $\mathcal{T} \rightarrow \|$ and $\mathcal{T} \rightarrow \perp$ were observed; at low shear rates, the parallel morphology was stable, and at higher shear rates the perpendicular morphology was stable. Later, Guo [31] used a similar model to study the transition from $\parallel\rightarrow\perp$; the kinetic mechanism was found to be through an undulation instability, partial breakup of monodomains, domain rotation, and recombination coupled to defect migration and annihilation. Liu *et al.* [32], used the standard DPD model of short block copolymers developed by Groot *et al.* [105–107]. They described a mechanism in which lamellar layers are distorted, and then evolve to the perpendicular orientation. The article also shows chevron instabilities in the strong segregation limit and sinusoidal instabilities in the weak segregation regimes for different values of the Flory-Huggins parameter (χN). Fraser *et al.* [108] used the same block copolymer DPD model to look at the stability of $\parallel$ and $\perp$. It was found that $\parallel$ has higher internal energy and a larger entropy production than $\perp$, and concluded that $\perp$ should be more stable at higher shear rates. Lísal and Brennan [109] performed a similar study to that of Fraser *et al.*, and found that there is also a metastable diagonal lamellar morphology. These articles employed a DPD thermostat because it is believed that hydrodynamic interactions can play a role in the mechanisms behind morphological transitions under non-equilibrium conditions [30, 31]. A review of simulation techniques for shearing polymer melts or solutions can be found in Rychkov [101].

The motivation for the present study is twofold: first, we aim to extend a coarse grained formalism for description of block copolymer assembly that has been particularly helpful under equilibrium to non-equilibrium situations. Eventually, we would like to investigate the dynamics of copolymer assembly on chemical nanopatterns [42, 110, 111]. Note that past reports on equilibrium Monte Carlo simulations using the model considered here have shown good agreement with experiments; [16, 25–29, 56, 81, 82] there is reason to expect that such agreement will continue in out-of-equilibrium situations. Second, we seek to investigate the behavior of copolymer lamellae under shear and determine the source of the discrepancies between the predictions of different theoretical approaches.

Specifically, in this work, we implement a particle-based theoretically informed block copolymer model[16, 25–29, 56, 81, 82] with Brownian dynamics and the Dissipative Particle Dynamics thermostat to examine its behavior under non-equilibrium molecular conditions, namely shear flow, using Lees-Edwards Boundary Conditions [51]. We examine the differences that arise when conservation of local momentum is enforced through DPD thermostats, and when Brownian dynamics approaches are employed.

3.2 Methods and Model

The coarse-grained model employed in this work has been described in the literature [16, 25–29, 56, 81, 82]; it takes into account the main characteristics of copolymers, including chain connectivity, compressibility, and the incompatibility of the monomers. Each chain is discretized into N beads; the position of the s^{th} bead on the i^{th} chain in denoted by $\mathbf{r}_i(s)$. The total Hamiltonian can be written as the sum of bonded contributions (H_b) and non-bonded contributions (H_{nb}):

$$H(\mathbf{r}_i(s)) = H_b(\mathbf{r}_i(s)) + H_{nb}[\phi_A, \phi_B] \tag{3.1}$$

where $H_b(r_i(s))$ is given by

$$\frac{H_b(r_i(s))}{k_B T} = \frac{3}{2}\sum_{i<j}\left(\frac{r_{ij}}{b}\right)^2 B_{ij} \tag{3.2}$$

and H_{nb} is given by

$$\frac{H_{nb}}{k_B T} = \sqrt{\mathcal{N}}\int_V \frac{dr}{R_e^3}\chi N \phi_A \phi_B + \frac{\kappa N}{2}(\phi_A + \phi_B)^2] \tag{3.3}$$

the sum in Equation 3.4 runs over all beads (Nn) (where n is the number of chains and N is the number of beads per chain), B_{ij} is either unity if there is a bond linking the beads or zero otherwise, $\phi_K(\mathbf{r})$ is the normalized local density of type A or B beads, ρ_0 is the number density of the beads, V is the volume, and $\sqrt{\overline{\mathcal{N}}}$ is the number of chains per unit chain volume, which can be extracted from experiments. The interdigitation number is defined by $\sqrt{\overline{\mathcal{N}}} = \rho_0 R_e^3/N$ [26], where R_e is the average end-to-end distance, and $b^2 = R_e^2/(N-1)$. Essentially, $\overline{\mathcal{N}}$ controls the strength of the fluctuations; it can be estimated from the molecular weight and melt density determined from experiments [78]. The strength of non-bonded interactions between a homopolymer of type A with a homopolymer of type B is determined by the Flory-Huggins parameter (χ), and κ ensures that there is a continuous density throughout the system (a description for the choice of κ is given in Pike *et al.* [25]).

By defining a density cloud ($\omega(\mathbf{r})$) around each particle's position, one can compute the beads' local densities ϕ_K. The integral in Equation 3.4 can therefore be written as a sum of pairwise interactions between beads,

$$U_{ij} = \frac{\sqrt{\overline{\mathcal{N}}}}{R_e^3}\left[\kappa N + \chi N(1-\delta_{KK})\right]\int_V \omega(\mathbf{r}-\mathbf{r_i})\omega(\mathbf{r}-\mathbf{r_j})dr \tag{3.4}$$

where K is either type A or B. The density cloud decays to zero after a cutoff distance r_{int}, which allows for each bead to have a sufficient number of interactions with neighbors, as determined in Detcheverry *et al.* and Pike *et al.* [25, 26]. Spherical step-like functions are used to determine the interactions, so the beads can be thought of as soft spheres where the pair-wise interaction energy is proportional to the overlapping volume of the density clouds. The density clouds are normalized to unity, so $\omega(\mathbf{r}) = C\tilde{\omega}(r)$ where $\tilde{\omega}(r) = 1$ if $r <= r_{int}$, $\tilde{\omega}(r) = 0$ if $r >= r_{int}$, and C is a normalization constant. Following Pike *et al.*, in our simulations each bead interacts on average with 14 beads.

The model described above can be implemented using Brownian dynamics; the evolution of the particles is described by

$$\gamma\frac{d\mathbf{r_i}}{dt} = \mathbf{f}_i^b(t) + \mathbf{f}_i^{nb} + \zeta_i(t) \tag{3.5}$$

where $\mathbf{r}_i$ is the position vector of bead i, γ is the friction coefficient, $\mathbf{f}_i^b$ and $\mathbf{f}_i^{nb}$ are the bonded and non-bonded forces on particle i, respectively, given by $\mathbf{f} = -\nabla U$, and ζ is a Gaussian random vector with zero mean, unit variance, and $\langle \zeta^{\mathbf{2}} \rangle = 2\gamma k_B T$. In the limit of the non-bonded interactions going to zero, the Brownian dynamics equation gives use to the Rouse model. A discussion of this implementation in equilibrium can be found in Ramírez-Hernández *et al.* [112].

The Brownian dynamics approach outlined above does not conserve momentum. Groot *et al.* [105, 106] used a DPD thermostat for block copolymers and showed that hydrodynamics plays an important role in the kinetics of microphase separation of hexagonally packed cylinders. Furthermore, previous theoretical work has shown that DPD reproduces the transition $\| \rightarrow \perp$. More generally, several reports have highlighted the importance of DPD thermostats in non-equilibrium flows [30, 31, 113]. The DPD model consists of the summation of conservative forces (F^C), noise (F^R), and dissipative forces (or friction) (F^D). The conservative forces for this paper are derived from the forces from the Hamiltonian in Equation 1. The random forces and dissipative forces on each particle, respectively, are given by

$$\begin{gathered}\mathbf{F}_i^R = \sigma \textstyle\sum_{i<j} \omega^R(\mathbf{r_{ij}})\hat{\mathbf{r}}_{ij}\zeta_{ij}/\sqrt{\delta t}, \\ \mathbf{F}_i^D = -\gamma \textstyle\sum_{i<j} \omega^D(\mathbf{r_{ij}})(v_{ij} \cdot \mathbf{r_{ij}})\hat{\mathbf{r}}_{ij}\end{gathered} \tag{3.6}$$

where ζ_{ij} is a random vector with zero mean and unit variance for a pair of particles (i, j), $\mathbf{v}_{ij} = \mathbf{v}_i - \mathbf{v}_j$, and $\mathbf{r_{ij}}$ is the vector between two beads. The weight function is given by

$$[\omega^R]^2 = \omega^D = \begin{cases} (1 - r/r_{int}), & r < r_{int} \\ \\ 0, & r \geq r_{int} \end{cases} \tag{3.7}$$

which is common in the DPD literature and $\sigma = \sqrt{2\gamma k_B T}$. As discussed in the literature, DPD gives the correct hydrodynamics [114, 115]. To evolve the beads in time, a modified

Velocity-Verlet algorithm is used according to

$$\begin{aligned}
\mathbf{r}_i(t+\delta t) &= \mathbf{r}_i(t) + \delta t \mathbf{v}_i(t) + \tfrac{1}{2}\delta t^2 \mathbf{f}_i(t) \\
\tilde{\mathbf{v}}_i(t+\delta t) &= \mathbf{v}_i(t) + \tfrac{1}{2}\delta t \mathbf{f}_i(t) \\
\mathbf{f}_i(t+\delta t) &= \mathbf{f}_i(\mathbf{r}_i(t+\delta t)), \tilde{\mathbf{v}}_i(t+\delta t)) \\
\mathbf{v}_i(t+\delta t) &= \tilde{\mathbf{v}}_i(t+\delta t) + \tfrac{1}{2}\delta t(\mathbf{f}_i(t) + \mathbf{f}_i(t+\delta t))
\end{aligned} \tag{3.8}$$

where δt is the time step, $\mathbf{v}_i$ is the velocity of bead i, $\tilde{\mathbf{v}}_i$ is the half-step velocity of the bead, and $\mathbf{f}_i$ is the sum of the conservative forces, random forces, and dissipative forces. A value of δt=0.01 is used for the simulations.

Common methods for including shear in simulations include the approach of Müller-Plathe [116] or the use of Lees-Edwards (LE) periodic boundary conditions [51]. Here we used LE periodic boundary conditions, where the boundary conditions dictate an average velocity gradient or shear rate. The gradient of the velocity profile is $\dot{\gamma} = dv_x/dr_z$. Figure 3.2 provides a schematic representation of the algorithm is shown. For the Brownian Dynamics case, the positions are updated by adding an external flow-field in the x direction,

$$\mathbf{f}_{i,x}^{drag} = \bar{\dot{\gamma}}\gamma\left(r_{i,z}(t) - \frac{L_z}{2}\right) \tag{3.9}$$

where $\bar{\dot{\gamma}} = V_D/L_z$ is the average shear rate and $V_D/2$ is the velocity at the top of the simulation box, $\dot{\gamma} = \frac{\partial v_x}{\partial z}$ is the local shear rate, L_z is the height of the simulation box in the z direction, and the total force on particle i is are now $\mathbf{f}_i = \mathbf{f}_i^b + \mathbf{f}_i^{nb} + \mathbf{f}_{i,x}^{drag}$. In what follows this method will be referred to as Brownian Dynamics Flow (BDF).

For the DPD thermostat, LE periodic boundary conditions were used to shear the block copolymers as follows. When a bead crosses the boundary in the z direction, the velocities

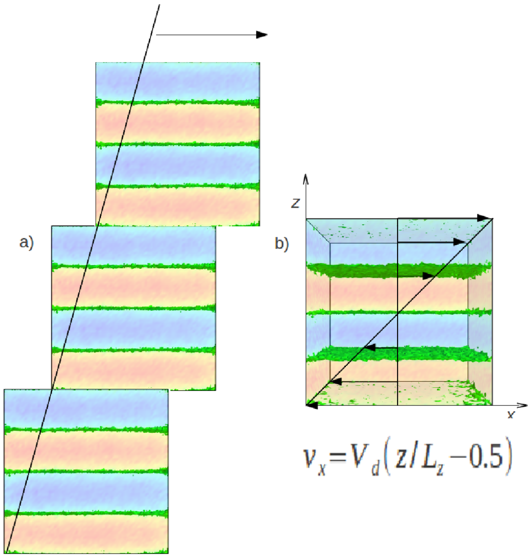

Figure 3.2: Schematic representation of the Lees-Edwards Periodic Boundary conditions. a) is a representation of how the system is implemented and b) is the final velocity profile. Figures were generated using an Open-Source Scientific Visualization Software, Mayavi2[1].

are updated in the x direction, but the y and z velocities remain the same:

$$v_{i,x}(t) = v_{i,x}(t) \pm V_D \tag{3.10}$$

where the positive sign is used when the beads cross in the negative z direction, and the negative sign is used when the beads cross in the positive z direction. This method is simply referred to as DPDT. An important difference between the methods used here is that in BDF a linear velocity profile is enforced, whereas in DPDT the velocity profile is induced by the LE periodic boundary conditions, and may not be linear.

Parameters: A 10K-b-10K polystyrene-b-polyisoprene near the ODT as in Bates *et al.* and Leist *et. al* [99, 117] block copolymer was modeled. This corresponds to $\sqrt{\mathcal{N}} = 58$, $\chi N = 15$, and $\kappa N = 15$. We choose $N = 32$. The relaxation times ($\tau = R_e^2/D$) are $\tau_{BDF} = 77.485$ R_e^2/D_0 and $\tau_{DPDT} = 87.98$ R_e^2/D_0, where $D_0 = k_BT/\gamma = 1$ where γ is the friction coefficient; and $\sigma = 3.0$. It should be noted that in contrast to models with steep excluded volume interactions, the friction comes from the thermostat (*i.e.* the soft non-bonded interactions do not generate significant friction). The prediction of the Rouse model's relaxation time is $\tau_{Rouse} = 88R_e^2/D_0$ in a disordered state.

3.3 Results and Discussion

When evolving the system with BDF, we started with three different lamellar configurations, namely parallel($\|$), perpendicular($\perp$), and transverse ($\mathcal{T}$), as seen in Figure 3.1. We performed simulations by increasing the shear rate for each of the three initial configurations. If the initial configuration was $\mathcal{T}$, and the shear rate was turned on, the final stable configuration was $\|$. At intermediate shear rates diagonal lamellae were found to be stable. At high shear rates, $\perp$ was found to be stable, as seen in 3.3 b and c. This is in agreement with experiments where the stable orientations under the influence of increasing shear rate are $\|$ and then $\perp$. However, for an initial configuration $\|$ or $\perp$, increasing the shear rate did not change the lamellar orientations. This is in contradiction with theoretical and experimental results that show a transition $\|\rightarrow\perp$ at high shear rates. For the initial configuration of $\mathcal{T}$, lamellae undergo a quick disordering transition, then a long reordering phase for both perpendicular and parallel orientations, where the disordered state can be seen in Figure 3.3d.

Next, the system was evolved with DPDT and the Velocity-Verlet algorithm from the same initial configurations. $\mathcal{T}$ is qualitatively similar to that obtained with BDF, where the stable configurations are a sinusoidal $\|$ (Figure 3.3a) and $\perp$ (Figure 3.4e). Since the block copolymers are in the weak segregation limit, they exhibit a sinusoidal final configuration, as in Liu *et al.* [32]. The mechanisms of formation, however, are slightly different. The reordering of the lamellar microstructures happens along the mechanism proposed in Lísal, illustrated in Figure 3.4, where the lamella break up and then reform. Major differences come in the changes in $\|$. At low shear rates the parallel morphology is maintained. However, at intermediate shear rates, a diagonal lamellar orientation is stable. The diagonal state is assumed to be a metastable state [31, 32]. The mechanism for the transition $\|\rightarrow\perp$ is

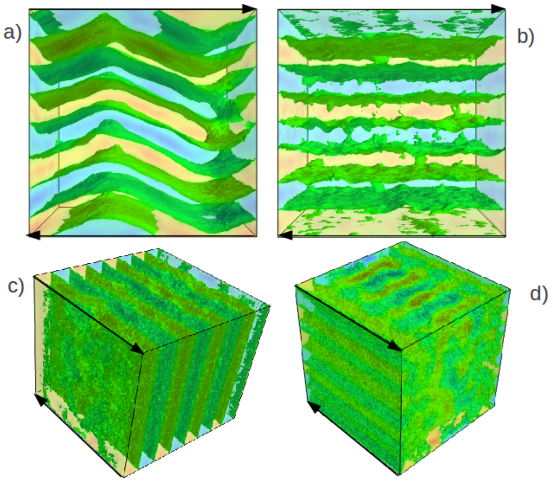

Figure 3.3: Final simulation snapshots of the initial configuration of $\mathcal{T}$. a) a sinusoidal '$\|$' using DPDT at Wi $= \bar{\dot{\gamma}}\tau = 0.70$ b)$\|$ using BDF at Wi $= 6.119$, and c) $\perp$ using DPDT and BDF (qualitatively similar results). d) A snapshot of $\mathcal{T}$ at Wi=6.119 after 1000 timesteps after shearing. Arrows represent shearing in the x direction. Figures were generated using an Open-Source Scientific Visualization Software, Mayavi2[1].

qualitatively similar to that observed in DPD studies with both the reverse non-equilibrium algorithm and Lees-Edwards algorithms [30–32, 108, 109]. Fluctuations in $\|$ eventually force the lamellae to break up and, through a long reorientation process, the lamellae form the final structures seen in Figure 3.4.

An interesting result is found in the velocity profiles along the gradient for BDF and DPDT. When examining the velocity profiles for $\perp$ and $\|$, there is a 'dip' in the velocity profile. For $\perp$, the velocity profile is linear, as in Guo and coworkers [30]. In our implementation, the velocity profile for $\|$ has 'dips' in it, localized at the interface between block A and block B. What this means is that the ends of the polymer chains are moving faster than the middle of the chain when compared to the linear velocity profile. This can be further explained by looking at different values of χN and the stress throughout the simulation box.

Two simulations were run at lower temperatures and a larger molecular weight to ensure the lamellae remain $\|$. The initial configurations of these simulations were lamellae in the

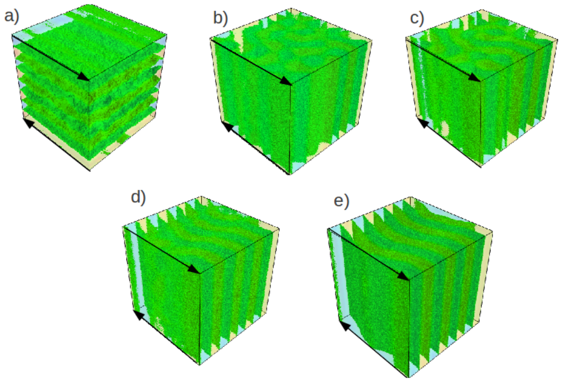

Figure 3.4: The mechanism for DPDT with $\parallel$ as the initial configuration. a) 20,000 timesteps, b) 35,000 timesteps, c) 40,000 timesteps, d) 50,000 timesteps, e) final configuration (70,000 timesteps) at Wi=31.67, and for systems with lengths $L_x = L_y = L_z = 4L_0$. Arrows represent shearing in the x direction. Figures were generated using an Open-Source Scientific Visualization Software, Mayavi2[1].

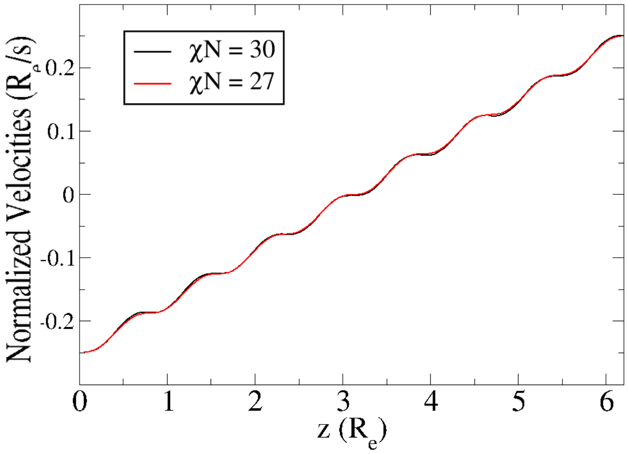

Figure 3.5: Velocity profiles throughout the simulation box for lengths $L_x = L_y = L_z = 4L_0$ in DPDT simulations.

parallel direction, with Wi $= \bar{\dot{\gamma}}\tau = 56.18$. The velocity profile exhibits larger 'dips' at larger values of χN, as seen in Figure 3.5. In Figure 3.6, a smaller box is used at the same shear rate with normalized length in the z direction, to accentuate the 'dips' for different values of χN. When heating the system, the $\parallel$ begin the transition to the diagonal lamellae, which is expected for this shear rate. If we examine xx, yy, zz, and xz components of the stress (σ_{xx},σ_{yy},σ_{zz},σ_{xz}), we can see one reason why the flip from $\parallel \rightarrow \perp$ occurs. The local stresses

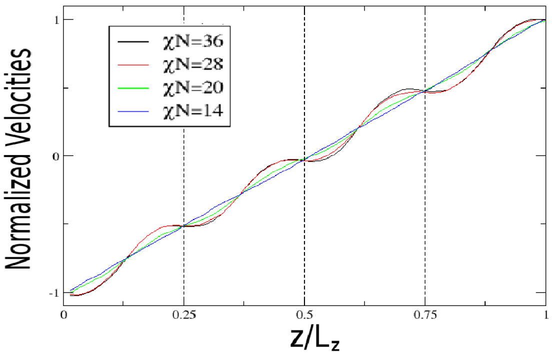

Figure 3.6: Velocity profiles throughout the simulation box for lengths $L_x = L_y = L_z = 2L_0$ and normalized in the z direction to accentuate the 'dips'. The dotted lines refer to the interfaces for DPDT.

are calculated from the following expression

$$\frac{\sigma_{\alpha\beta}}{k_BT} = \sum_i \delta(\mathbf{r}-\mathbf{r}_i)\delta_{\alpha\beta} + \sum_{j>i} r_{ij,\alpha} f_{ij,\beta} \int_0^1 ds\delta(\mathbf{r}-\mathbf{r}_i - s\mathbf{r}_{ij}) \tag{3.11}$$

where $f_{ij,\beta}$ is the force between bead i and j from the thermostat, bonded, and non-bonded potential; α, $\beta \in \{x, y, z\}$; the global stress is $\sigma_{\alpha\beta} = \int_V d\mathbf{r}\sigma_{\alpha\beta}(\mathbf{r})/V$ and the pressure is $Tr(\sigma)/3$.

In Figure 3.7a, we show plots of the xx, yy, and zz components of the stress near the interface with DPD. As expected, in the absence of shear, the local stress normal to the the interfaces in a lamella forming melt is constant, and the tangential stresses exhibit both a minimum and a maximum [25, 118, 119]. When increasing the shear rate to Wi=56.18 (Figure 3.7b), distinc minima in σ_{xz} arise at the interface. Although one would initially expect the σ_{xz} profile to be constant throughout the simulation box, in the Appendix we present simple continuum mechanics arguments to justify the observation of the oscillations. There is tumbling motion in the block copolymers due to a correlation of the x and z velocity components; such motion is apparent in the velocity vector fields shown in Figure 3.8. When Wi $\rightarrow 0$, the oscillations in $\sigma_{xz}/\bar{\dot{\gamma}}$ vanish (this is discussed in the Appendix). The magnitude

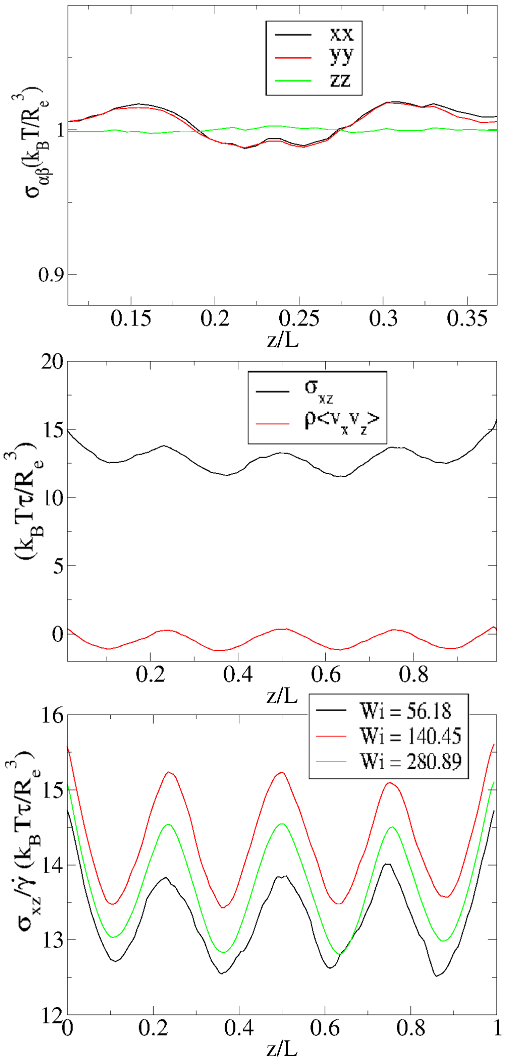

Figure 3.7: Stress plots for a) σ_{xx},σ_{yy},σ_{zz} at the interface 0.225 z/L_Z without shear b)σ_{xz} and $\rho\langle v_x v_z\rangle$ for Wi=56.18 c)σ_{xz} for increasing shear rates from Wi=56.18 to Wi=280.89. The interfaces are at 0, 0.225, 0.445, and 0.75 for this system

of the oscillations decreases as we decrease the Wi number. A slower moving block copolymer would have a smaller gradient in the velocity profile, which can be seen in the velocity profiles. If we compare the stress plots of the parallel lamellae to the perpendicular lamellae, we can see that the stresses are constant throughout the simulation box (data not shown). This is in agreement with Chen *et al.*, who pointed out that the polymers are being stretched and have an external stress; to relax, the block copolymers flip to the perpendicular orientation.

Finally, the angles between the block copolymer blocks were analyzed. The vector for each block was calculated from the covalent bond between blocks A and B to the center of mass of each block. As expected, 80% of the angles were between 150 and 180 degrees. This is consistent with results for sheared homopolymers in solution, where the polymers align with the velocity profile [120, 121].

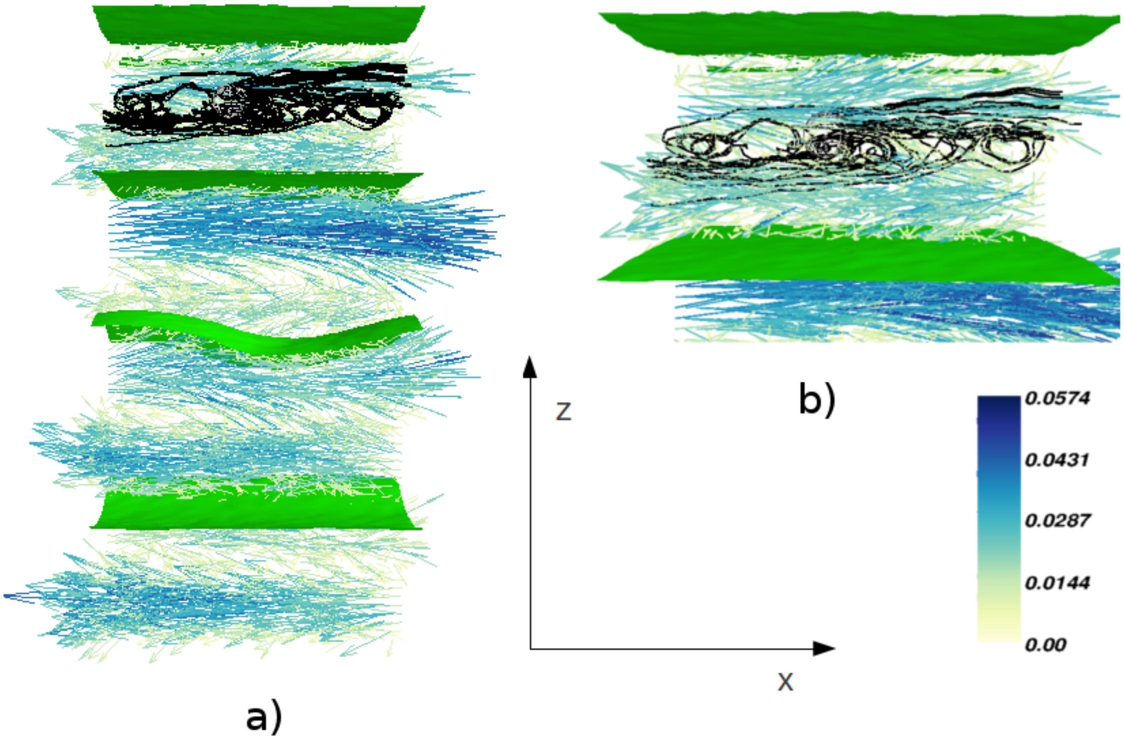

Figure 3.8: Velocity vector field for Wi=56.18. The legend from cream to blue corresponds to the magnitude of the velocity vectors (the average velocity gradient has been subtracted $v_i = v_i - \bar{\dot{\gamma}}\gamma\left(r_{i,z}(t) - \frac{L_z}{2}\right)$), green planes show the interfaces between A and B blocks, and black lines represent several stream lines (calculated according to [1]). a) Full simulation box of $\perp$ lamellae as in Figure 3.7 and b) expanded view of the top of the simulation box.

To examine the oscillations in σ_{xz}, one should look at the conservation of momentum. The Navier-Stokes equation is as follows:

$$\rho\frac{\partial \mathbf{v}}{\partial t} + \rho\mathbf{v}\cdot\nabla\mathbf{v} = \nabla\cdot\sigma + \mathbf{f} \tag{3.12}$$

where $\mathbf{p}$ is the momentum, $\mathbf{v}(r)$ is the velocity field, ρ is the constant mass density, $\sigma = -p\mathbf{I} + \pi$ is the stress tensor, and $\mathbf{f}$ are the body forces. In our case $\frac{\partial \mathbf{v}}{\partial t} = 0$ because of steady state and $\mathbf{f} = \mathbf{0}$ because the flow is driven by boundary conditions. The hydrodynamic velocity field $\langle \mathbf{v} \rangle$ it is obtained averaging over a sufficiently large volume element or a sufficiently long time interval, so thermal fluctuations are averaged out. If we look at a microscopic velocity field, as in our simulations, one can average Equation 12.

$$\rho\langle \mathbf{v} \cdot \nabla \mathbf{v} \rangle = \rho\langle v_x \frac{\partial v_x}{\partial x} + v_y \frac{\partial v_x}{\partial y} + v_z \frac{\partial v_x}{\partial z} \rangle = \frac{\partial}{\partial z} \langle \sigma_{zx} \rangle \tag{3.13}$$

or

$$\frac{\partial}{\partial z} \left(\langle \sigma_{zx} \rangle - \rho \langle v_x v_y \rangle \right) = \rho \langle \frac{1}{2} v_x \frac{\partial v_x^2}{\partial x} + v_x \frac{\partial v_y}{\partial y} - v_x \frac{\partial v_z}{\partial z} \rangle \tag{3.14}$$

To linear order in velocity, the shear stress, $\langle \sigma_{zx} \rangle$, is independent of the spatial coordinate, z. If one extrapolates the simulation to vanishing shear rate, $\bar{\dot{\gamma}} \to 0$, and plots $\langle \sigma_{zx} \rangle / \bar{\dot{\gamma}}$, where $\bar{\dot{\gamma}}$ is the spatially averaged shear rate, this quantity should become constant. One can also define a local viscosity, $\eta(z)$, from

$$\frac{\langle \sigma_{zx} \rangle}{\bar{\dot{\gamma}}} = \eta(z) \frac{1}{\bar{\dot{\gamma}}} \frac{\partial v_x}{\partial z} \tag{3.15}$$

This implies that the shear stress is independent from z in the limit $\bar{\dot{\gamma}} \to 0$, and that the spatial dependencies of the local viscosity and the velocity gradient cancel. However, for higher shear rates, there are corrections according to Equation 3.14, which are correlations between different velocity directions. In equilibrium, $\langle v_i v_j \rangle = \frac{k_B T}{m} \delta_{ij}$; therefore corrections have to be induced by the shear and this observation is compatible with the effect being second-order in v.

If we examine the right-hand side of Equation 3.14, the term proportional to $\frac{\partial \langle v_x^2 \rangle}{\partial x}$ is independent from the spatial position because $\langle v_x^2 \rangle = k_B T/m$ is establishing the equilibrium value from the thermostat. Second, both v_y and any spatial dependence along the y-directions are small for lamellae oriented with the normal in the z direction and flow in x-direction. Lastly, we argue that the correlation induced by the shear flow gives rise to a tumbling motion of the blocks. This tumbling motion has been observed in isolated macromolecules in shear flow and in single molecules tethered to surface. Given the soft interactions which suppress both static local fluid-like correlations, *i.e.*, packing, as well as any entanglement effects, this tumbling motions also occurs in polymer brushes [122]. This rotational motion gives rise to a perturbation of the velocity field that is approximately proportional to $\mathbf{e}_y \times \mathbf{r}$ and, in this case, the term $\partial v_z/\partial z$ vanishes. Canceling these terms and integrating Equation 3.14 gives the following:

$$\langle \sigma_{zx} \rangle \approx \rho \langle v_x v_z \rangle + const \tag{3.16}$$

The result of Equation 16 is exactly what is seen in Figure 3.7b.

Lastly, we note that Noguchi and Gompper [123] have shown that for the DPD thermostat to provide local equilibrium conditions in steady shear, $\bar{\dot{\gamma}} r_{cut} \ll \sqrt{k_B T/m}$, must be satisfied. Using the cut off distance from our calculations, we find that according to the requirement, the highest Wi number should be 6.42. Our simulations for the transition from $\| \rightarrow \perp$ are carried out at Wi=29.0 to 31.67. To examine that we do not have large fluctuations in the thermostat, we calculated $k_B T(z)$, for Wi=56.18 and Wi=280.89. Both of these values are much larger than the Wi number used for the transition from $\| \rightarrow \perp$. In Figure 3.9, there are oscillations in $k_B T$, and there is a correlation with the velocity profiles. Lower values of the velocity at the interface and larger velocities in the middle of the block. Even at these high shear rates, the oscillations are about one to two percent of the average or less. Moreover, the oscillations become larger at higher shear rates. At a Wi=31.67, the temperature of the system is 1.014; therefore, we believe the thermostat works properly in these simulations for the transition from $\| \rightarrow \perp$.

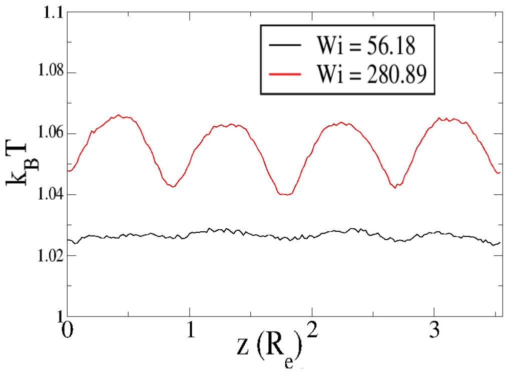

Figure 3.9: The local distributions of $k_B T$ versus the z-direction. The interfaces are at 0.9, 1.8, and 2.7 R_e.

3.4 Conclusions

The transitions from $\mathcal{T} \rightarrow \|$ and $\mathcal{T} \rightarrow \perp$ were captured with both BDF and DPDT. The transition from $\| \rightarrow \perp$ in the BDF case does not occur, which is in contradiction to literature reports, both experimental and theoretical. With the enforcement of conservation of momentum through the DPD thermostat, the transition from $\| \rightarrow \perp$ does occur.

The key differences between our calculations and previous DPD simulations [32, 108, 109] reside in the densities of the system, the interaction between like and unlike beads, the length of the molecules, and the level of discretization. With respect to the densities, the $\sqrt{\mathcal{N}}$ used in previous DPD studies is equivalent to 0.3, while the $\sqrt{\mathcal{N}}$ used in these simulations is 58; this means the systems in the present paper are about 193 times more dense and are experimentally relevant. The discretization of the chains (N) was at most 10 for past DPD studies, and it is 32 for the simulations reported here. This level of coarse-graining may have prevented previous studies from observing the tumbling motion because it relies on thermal fluctuations of the molecular conformations. Five beads per block may not be sufficient to adequately capture fluctuations of the molecular shape. The Theoretically Informed Course Grained model also uses the Hamiltonian from Helfand [77], in contrast to a repulsive term for non-bonded forces employed in previous DPD studies. Guo [30, 31], for example, used an amphiphilic model consisting of only four beads per chain, which would be coarse grained on a level too large for our purposes. Also, Guo *et al.* adopted a LJ model.

The Theoretically Informed Coarse Grained model gives useful insights into the reasons why the flip from $\parallel \rightarrow \perp$ occurs. When shearing $\parallel$ at a low temperature, the stresses along the interface are larger than the stresses in the middle of the lamellae. These results show that the 'dips' in the velocity profile for $\parallel$ are not artifacts and explain why the beads are moving faster or slower: *i.e.* it shows why $\parallel$ is not stable at higher shear rates. It is also hypothesized that the inclusion of the local conservation of momentum allows for the transition $\parallel \rightarrow \perp$. Finally, we note that the simulations presented here are for unentangled block copolymers near the Order Disorder Transition and Rouse chains. In the future, we plan to explore the flip with entangled block copolymers, for example in the PEP-b-PEE block copolymers of Chen *et al.* [102].

CHAPTER 4

A MULTICHAIN POLYMER SLIP-SPRING MODEL WITH FLUCTUATING NUMBER OF ENTANGLEMENTS

Coarse grained simulation approaches represent a powerful tool to predict the equilibrium and far-from-equilibrium behavior of multicomponent polymer systems. However, most of those approaches relay on soft intermolecular interactions, thus the local non-crossability is violated and dynamical phenomena associated to topological constraints is not captured. Sip-spring models are capable to reincorporate the effect of those topological interactions at a low computational cost. In this work, we extend our previously introduced multichain slip-spring model such that it, correctly, incorporates the effect of the fluctuating environment in which a polymer segment is immersed. We use this modified version to obtain the equation of state associated to the slip-springs and compare it to an analytical expression deduced by Chappa et al. The behavior of the model is also explored for the case where polymer melts are confined into thin films. The inhomogeneous distribution of polymer segments, and the corresponding inhomogeneities of density fluctuations, are reflected on the spatial slip-spring distribution.

4.1 Introduction

Coarse-grained approaches are a powerful methodology for modeling the behavior of soft condensed matter systems. These approaches allow to explore the wide spectrum of spatial and temporal scales associated with the collective behavior of such soft materials. In particular, self-assembly processes operate at scales that are prohibitively long for a fully atomistic description, thus coarse-grained modeling can provide insights into the physical principles behind of such self-organization. By coarsening the description of a system, the number of degrees of freedom is reduced and finer details ignored. At same time, effective interactions between the surviving interacting sites become soft, *i.e.* the interaction energy between two interacting sites remains finite in the limit $r \rightarrow 0$, where r is the distance between two coarse-grained (CG) particles. Therefore, by ignoring the finer details regarding the local non-crossability between molecules, faster equilibration of systems with mesoscopic, or even macroscopic, length scales can be achieved. Kinetic and dynamical processes can also be studied by using these approaches, and the agreement with experimental observations highlights how powerful these simulation approaches are. However, there are systems for which those non-crossability microscopic details have consequences at large scale, specifically, high molecular weight polymer melts and concentrated solutions. For those cases, topological constraints play a very important role regarding the mechanical properties and dynamics of such a systems. Therefore, phenomenological top-down approaches that reincorporate the effect of those topological interactions with low computational cost are highly valued, as such approaches would allow to explore the large time and length scale dynamics and kinetics of complex macromolecular systems and their processes, i. e. hierarchical self-organization in- and out-equilibrium.

Among the different attempts to reincorporate such topological constraints at a coarse grained level, there are some that propose to use explicit entanglements at the two-molecule level. In particular, we have recently reported a new simulation approach able to describe the linear and non-linear rheology of entangled polymer melts[124]. This approach relies on a many-chain representation, and introduces the topological effects that arise from the non-crossability of molecules through effective fluctuating interactions, mediated by slip-springs (SS), between neighboring pairs of macromolecules. The total number of slip-springs is not constant but, instead, it is controlled through a chemical potential that determines the average molecular weight between entanglements. Our results were shown to be in quantitative agreement with experimental data, and suggest that the proposed formalism may also be used to describe the dynamics of inhomogeneous systems, such as composites and block copolymers. We also made a connection between our model and the single-chain mean-field models. The reported results are highly encouraging, as our approach and the single-chain formalisms could be integrated to perform systematic coarse-graining.

As encouraging as our previous results are, however, there was a strong assumption regarding the process of creation and destruction of entanglements between a given pair of molecules, namely, the local environment around a specific polymer segment was considered non-fluctuating. Such assumption is valid in single-chain descriptions but it is not in particle-based simulation approaches. The consequences of such assumption are minor for homogeneous systems, as the homopolymer melts considered in our previous report. But such a fluctuations should be taken into account to describe inhomogeneous systems, such as phase segregated block copolymers or thin films. In this work, we extend our previous model such that it incorporates the effect of the fluctuating environment in which a polymer segment is immersed. We use this new version to obtain the equation of state associated to the slip-springs and compare it to an analytical expression deduced by Chappa et al. We also explore inhomogeneous systems where confinement and phase segregation take place.

4.2 Model and Simulation Approach

The general details of our "Theoretically Informed Entanglement Polymer Simulations," or TIEPOS approach, have been described in our previous report. Here we provide with a short summary of the model and approach, highlighting the important differences. Let's consider a A-B polymer blend composed by $N_c = n_A + n_B$ macromolecules in a volume V at temperature T. The polymers are represented by the discretized Gaussian chain model and each macromolecule is composed of N_α beads, $\alpha \in [1, N_c]$. The system configurations are defined by giving the coordinates of all polymer segments $\{\mathbf{r}_i(s)\}$ at different times, where $\mathbf{r}_i(s)$ is the position of the s^{th} bead in the i^{th} chain. The intra-molecular interactions are given by $\beta\mathcal{H}_b = \frac{3}{2}\sum_{i=1}^{N_c}\sum_{s=1}^{N_i-1}[\mathbf{r}_i(s+1) - \mathbf{r}_i(s)]^2/b^2$, where b^2 is the mean squared bond length of an ideal chain, $\beta^{-1} = k_BT$, and k_B is the Boltzmann constant. Generalizations to more complex situations, including blends of polymers with different bond lengths or chain stiffness, are straightforward. The inter-molecular interactions are expressed as a functional of the local densities $\phi_{\mathrm{A,B}}(\mathbf{r})$:

$$\beta\mathcal{H}_{\mathrm{nb}} = \rho \int_V \mathrm{d}\mathbf{r} \left[\chi\phi_A\phi_B + \frac{\kappa}{2}(\phi_A + \phi_B)^2\right], \tag{4.1}$$

where ρ is the bead number density. The repulsion between unlike monomers, quantified by the Flory-Huggins parameter χ, is represented by the first term in the functional. A finite melt compressibility is prescribed by the second term, which corresponds to Helfand's quadratic approximation, where the parameter κ is related to the inverse isothermal compressibility. By regularizing the scalar density fields, $\phi_\alpha(\mathbf{r})$, employing a density cloud $w(\mathbf{r})$ associated with each interacting segment of the polymer chains, it is possible to transform the field-based description in Eq. 4.1 into a particle-based representation with a pairwise interaction potential, $\beta\mathcal{H}_{nb} = \sum_{i<j} U(\mathbf{r}_{ij})$, where the sum runs over all polymer segments in the system. These intra- and inter-molecular interactions are soft, thus entangled dynamics are not captured and we resort to slip-springs to represent such topological interactions.

The entanglements are represented by effective fluctuating interactions, mediated by slip-springs (SS). The SS consists of two anchoring units that move along different chain contours, and connect the respective polymer segments via a spring: $\beta u_{ss} = \frac{3}{2}[\mathbf{R}_k - \mathbf{R}_{n_k}]^2/b_{ss}^2$, where $\mathbf{R}_k$ denotates the position of the kth anchoring unit and n_k denotes its partner. b_{ss} characterizes the strength of the spring and is chosen as $b_{ss} = b$. The SS can only hop between polymer beads, and only one SS occupies a given segment. The total number of SS fluctuates and their number is controlled by a chemical potential μ, thus defining the average number of entanglements per chain, $\langle Z\rangle$. To initialize the SS configuration, for each SS pair, a polymer bead is randomly chosen and the first anchoring unit attached to that segment. Then, a nearby segment is chosen to place the partner anchoring unit, in such a way as to generate a Boltzmann distribution of links.

The time evolution of system configuration is performed by using a hybrid scheme, where polymer configurations are updated via dynamic simulations during a short time interval, τ_{ss}, and SS configurations are updated via Monte Carlo moves at the end of such time interval. We note here, that the slip-springs can be updated in a variety of ways, more generally, one could use a stochastic variable, $\hat{\tau}_{ss}$, with an arbitrary probability distribution $\Psi(\hat{\tau}_{ss})$, and use this function to generate a set of $\hat{\tau}_{ss}$'s and update slip-springs after these different waiting times. Here, we have opted for the simplest possible scheme, with $\Psi(\hat{\tau}_{ss}) = \delta(\hat{\tau}_{ss} - \tau_{ss})$ as this choice provides good agreement with experiments. In this work, for simplicity, we adopt a Brownian dynamics approach to evolve polymer segments. Thus, the time evolution of configuration $\{\mathbf{r}_j\}$ is governed by

$$\gamma \frac{\mathrm{d}\mathbf{r}_j(t)}{\mathrm{d}t} = \mathbf{f}_j^{\mathrm{b}}(t) + \mathbf{f}_j^{\mathrm{nb}}(t) + \mathbf{f}_j^{\mathrm{ss}}(t) + \boldsymbol{\xi}_j(t), \tag{4.2}$$

where $\mathbf{f}_j^{\mathrm{b}}$ and $\mathbf{f}_j^{\mathrm{nb}}$ are the intra- and intermolecular forces acting on polymer segment j, and $\mathbf{f}_j^{\mathrm{ss}}$ is the force associated with the slip-springs. $\boldsymbol{\xi}_j$ represents the stochastic influence of the coarse-grained microscopic degrees of freedom and satisfies the fluctuation-dissipation relation: $\langle \xi_{i\alpha}(t_1)\xi_{j\beta}(t_2)\rangle = 2\gamma k_{\mathrm{B}} T \delta_{ij}\delta_{\alpha\beta}\delta(t_1 - t_2)$, where $\alpha, \beta = x, y, z$, and γ is the friction coefficient.

During the SS configuration update, one performs $N_{ss}(t) + 2N_c$ attempts to update all SS present at that time t, $N_{ss}(t)$, as well as to create new SS at chain ends. For each attempt, an existing SS is selected with probability P_{SS}, or a chain-end is chosen randomly with probability $P_{ch} = 1 - P_{SS}$. Then, one of the following MC moves is attempted:

1 A *hopping* move, which involves the transfer of one end of a slip-spring from one polymer segment to a neighboring one, along the same polymer. We propose to move in one or the other direction along the chain with equal probability. This move is accepted with probability $p = \min(1, e^{-\beta \Delta u_{ss}})$, where Δu_{ss} is the difference on the slip-spring energy between the trial and old configuration.

2 A *creation* move creates a new slip-spring pair by adding a new ring to a randomly selected unoccupied chain end. The location of the ring's partner is selected from all M unoccupied polymer beads within a radius R_c with probability $e^{-\beta u_{ss}(r_j)}/\mathcal{W}$, where $\mathcal{W} = \sum_{k=1}^{M} e^{-\beta u_{ss}(r_k)}$. This move is accepted with probability $p = \min\left(1, \frac{P_{SS}}{P_{ch}} \frac{Nc}{2(N_{ss}+1)} \beta_e^{-1} \mathcal{W}\right)$.

3 A *destruction* move involves deletion of an existing slip-spring pair if one of the rings reaches the chain end, and moves out of the contour with probability 1/2. This move is accepted with probability $p = \min\left(1, \frac{P_{ch}}{P_{SS}} \frac{2N_{ss}}{Nc} \beta_e \mathcal{W}^{-1}\right)$. Here, $\mathcal{W} = e^{-\beta u_{ss}(r_1)} + \sum_{k=2}^{M} e^{-\beta u_{ss}(r_k)}$, where r_1 is the bond length associated to the slip-spring to be destroyed.

where $\beta_e = e^{-\beta\mu}$. Thus, the value of the chemical potential dictates the average number of slip-springs per chain. Note that the main relaxation mechanisms of entangled polymers are incorporated naturally in this approach: contour length fluctuations, reptation, and constraint release.

The important point to highlight here is the following: In our many chain model, at each instant of time there is a fluctuating discrete number of possible neighbors to anchor the other end of a slip-spring, also the microstates associated to those neighboring beads change from one time to another. All these microscopic details are encoded in $\mathcal{W}$, which is, therefore, a fluctuating quantity. Note that if there were not fluctuations in the local environment, as in the case of single-chain models, then $\mathcal{W}$ will be a constant, let's say $\mathcal{W}_o$, and could be adsorbed into β_e, thus renormalizing the SS chemical potential, i. e. $\mu' = \mu + \beta^{-1} \ln \mathcal{W}_o$. In our previous report we assumed the latter was the case, but this assumption it is not satisfied in our particle-based description of the polymer systems, which naturally includes fluctuations. Strictly speaking that assumption leads to incorrect sampling of the grand canonical ensemble associated to the slip-springs. However, the consequences of such assumption are minor for homogeneous systems, as the homopolymer melts considered in our previous report. But, it could have important consequences on inhomogeneous systems such as phase segregated block copolymers, thin films or solutions. The current implementation of the model correctly incorporates such microscopic fluctuations, and thus, $\mathcal{W}$ is a fluctuating scalar field, both in space as time.

4.3 Results

4.3.1 Homogeneous Systems

In this section we will explore the consequences of incorporating a fluctuating $\mathcal{W}$ into our multichain description of homopolymers, as indicated in the Methods section. We will compare the results with the scheme presented in our previous report. Note that $\mathcal{W}$ depends on particle density ρ, the higher number density is the less fluctuating $\mathcal{W}$ would be. In our previous report $\mathcal{W}$ was assumed to be a constant and plays no role on the acceptance probabilities, therefore, it is expected that the average number of slip-spring per chain $\langle Z \rangle$ would be insensible to changes in particle density in that scheme. On the other hand, the correct set of acceptance rules in this work, contain $\mathcal{W}$ on them, thus number density will affect the resulting $\langle Z \rangle$.

Thus, we fix the value of the chemical potential in both schemes and vary the polymer bead density. It is important to remark that the chemical potential in both schemes has not the same numerical value. Figure 4.1 shows $\langle Z \rangle$ as a function of density ρ. Indeed, our previous acceptance rules give a number of slip-springs per chain that do not depend on the bead density for large enough values (green dashed curve). However, the new set of acceptance rules gives place to a monotonic dependence on ρ. In fact, for relatively small densities, a linear dependence is found, which agrees with predictions and simulation results reported in Ref.[125] for a similar model as the one presented in here. One key difference between the model in Ref. [125] and ours, is that a single segment can be occupied by any number of SS, even with the same SS-coupled bead. In our case only one SS can be attached to a given polymer segment. Interestingly, the curve $\langle Z \rangle$ vs ρ, departs from a linear relationship for large densities. An explanation of this behavior can be obtained by taking a look into the analytical prediction for the SS equation of state derived in Ref.[125], which reads:

$$\langle Z \rangle = \frac{\rho}{\beta_e N_c} \left(N_c N - 3 \right) \int \mathrm{d}\mathbf{r}\, g\left(\mathbf{r}\right) e^{-\beta u_{ss}(\mathbf{r})}, \tag{4.3}$$

where $g(\mathbf{r})$ is the slip-spring pair correlation function, which only includes pairs of segments that can be connected by a slip-spring. Note, in particular, that if the melt's microscopic structure does not depends on density, i.e. if $g(r)$ is not affected by changing ρ, then for fixed chemical potential, $\langle Z \rangle$ grows linearly with ρ. However, if by changing ρ there is a change on the slip-spring pair correlation function, then a non-linear dependence should be expected. We computed the slip-spring pair correlation function for different particle densities. In Figure 4.2 we show $g(r)$ for two extreme cases: $\rho = 400/R_e^3$ and $\rho = 8000/R_e^3$. As can be seen, the local microscopic structure has a strong dependence on the particle density, therefore affecting the number of SS per chain, inducing a non-linear dependence on density.

Then, we keep number density fixed at a given value ($\rho = 1798 R_e^3$) and explore how $\langle Z \rangle$ is affected by the chemical potential. As reported in Figure 4.3, a monotonic dependence on the chemical potential is obtained. Again the growth of $\langle Z \rangle$ with μ agrees with that expected by Eq. 4.3. However, in this case too, a linear relationship was reported in Ref. [125]. The origin of this discrepancy between both approaches relies on one key difference: first, as mentioned above, in our approach each polymer bead can be occupied by only one slip-spring ("fermionic" case), whereas in Ref. [125] there is not restriction on the number of SS on a bead ("bosonic" model). Now, at a fixed density, the incorporation of slip-springs has not effect on the microscopic structure of the melt, even for large values of SS chemical potential (see Figure 4.4). Therefore, as the chemical potential is increased, the number of available unoccupied beads decreases given place to a slower growth of $\langle Z \rangle$ with μ. Whereas in model of Ref. [125] any number of SS on a single bead is permitted, thus increasing μ leads to more SS that can be accommodated between any neighboring pair of segments.

We conclude this section by comparing the analytical equation of state obtained for the many-chain system (Eq. 4.3) with that predicted by the single-chain theory of Schieber et al. In the latter theory, for discrete chains, the equation of state reads:

$$\langle Z \rangle = \frac{N}{\beta_e^{sc} + 1}, \tag{4.4}$$

where $\beta_e^{sc} = e^{-\beta\mu^{sc}}$, the superscript "sc" refers to the single-chain prediction, and, β_e^{sc} is chosen to be equal to the average number of beads between entanglements, N_e. Thus, for weakly entangled melts, this equation of state can be approximated by $\langle Z \rangle \approx \frac{N}{\beta_e^{sc}}$. On the other, for large systems Eq. 4.3 can be approximated by

$$\langle Z \rangle = \frac{N}{\beta_e} \langle \mathcal{W}(\rho) \rangle, \tag{4.5}$$

where

$$\langle \mathcal{W}(\rho) \rangle = \int \mathrm{d}\mathbf{r}\, \rho\, g(\mathbf{r})\, e^{-\beta u_{ss}(\mathbf{r})}, \tag{4.6}$$

is the average of the Rosenbluth factor defined in the creation-destruction rules described above. In the case of homogeneous systems $\langle \mathcal{W}(\rho) \rangle$ is independent of space and time. Thus, for weakly entangled homopolymers in bulk, we can identify $\beta_e^{sc} = \beta_e \langle \mathcal{W}(\rho) \rangle^{-1}$, i.e. the chemical potentials are related by $\mu^{sc} = \mu + k_B T \ln \langle \mathcal{W}(\rho) \rangle$. To corroborate this approximated relationship, first we plot the data in Figure 4.3 in terms of $\beta_e = \exp(-\beta\mu)$. This is shown in main panel of Figure 4.5. As can be seen a very similar dependence of $\langle Z \rangle$ on β_e is obtained (see Figure 2 in Ref. [1]), but the latter having quite different numerical values. Then, we use the time average of $\mathcal{W}$ sampled during the simulations, $\widehat{\mathcal{W}}$, and plot $\langle Z \rangle$ vs $\mu + k_B T \ln \widehat{\mathcal{W}}$, the resulting curve is presented in the inset of Figure 4.5 along with the equation of state predicted by the single-chain theory, Eq. 4.4. As can be seen, the simulations follows the analytical predictions, even for systems with small β_e^{sc}. Therefore, for homogeneous systems the results presented in Ref. [1] are very good approximations to the results obtained using the correct creation-destruction rules reported in here. However, in inhomogeneous systems the spatiotemporal character of $\mathcal{W}(r, t; \mu)$ will affect the creation-destruction rules locally, allowing for inhomogeneous entanglement distribution, as expected for example, in phase segregated block copolymers.

4.4 Conclusions

In this report we have extended our previous multichain slip-spring model with fluctuating number of entanglements such that it now correctly, incorporates the effect of the fluctuating environment in which a polymer segment is immersed. We have used this modified version to obtain the equation of state associated to the slip-springs and compare it to an analytical expression deduced previously. The formalism was used to study the effect of confinement into thin films, where segment density profiles and chain configurations are modified by the confinement. These inhomogeneities are reflected on the spatial distribution of slip-springs.

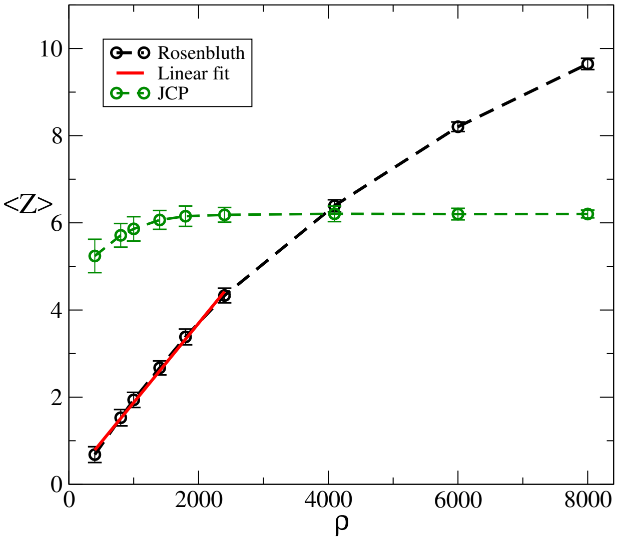

Figure 4.1: Average number of entanglements per chain, $\langle Z \rangle$, as a function of ρ. Green circles are obtained using the previous acceptance rules for the creation-destruction processes, while black circles are simulation results obtained by using the correct rules described on the text. Chemical potential differ in numerical value in both cases, but the rest of physical parameters are the same as those used in Ref. [1]. The red curve is a linear fit to the small density data.

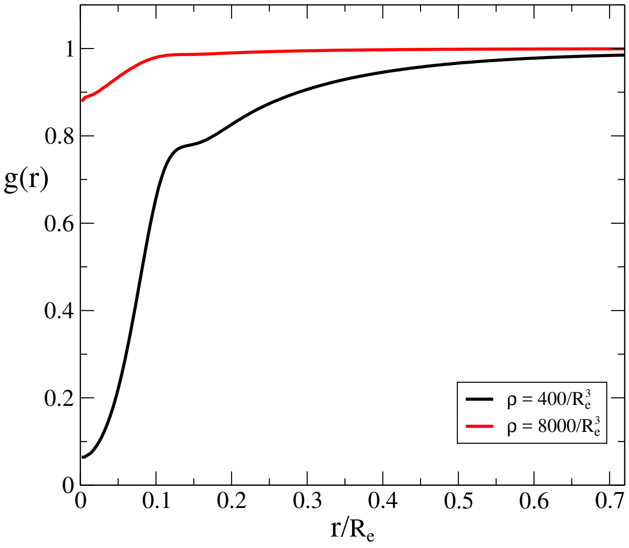

Figure 4.2: Slip-spring pair correlation function $g(r)$ for two different number densities, as indicated on the labels.

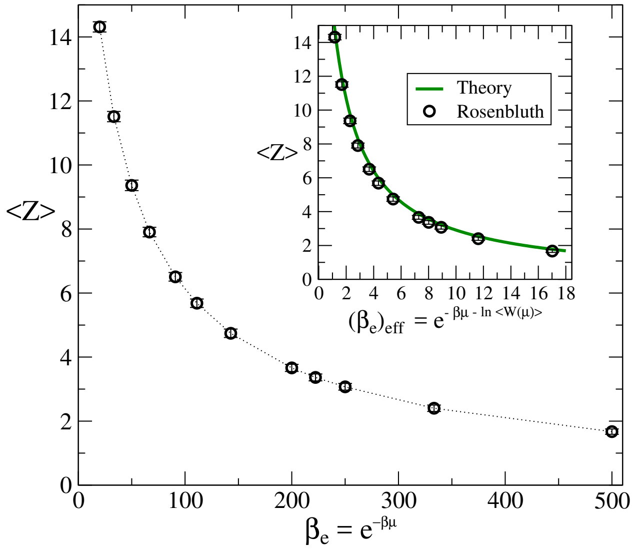

Figure 4.3: Average number of entanglements per chain, $\langle Z \rangle$, as a function of $\exp(\beta\mu)$. Results obtained by using the algorithm described in this work. Density is fixed at $\rho = 1798R_e^3$.

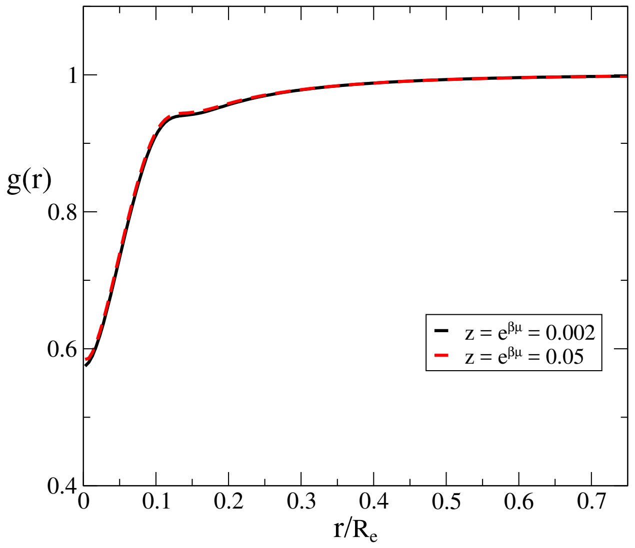

Figure 4.4: Slip-spring pair correlation function $g(r)$ for two different chemical potential values at $\rho = 1798R_e^3$.

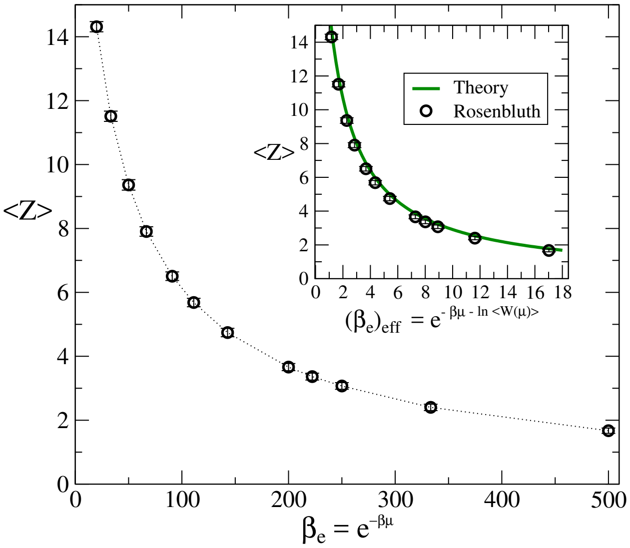

Figure 4.5: *Main panel*: Average number of entanglements per chain, $\langle Z \rangle$, as a function of β_e. *Inset*: Average number of entanglements per chain, $\langle Z \rangle$, as a function of an effective chemical potential. Line is theoretical prediction and symbols are numerical simulation results. $N = 32$ and $\rho = 1798 R_e^3$.

CHAPTER 5

A DETAILED EXAMINATION OF THE TOPOLOGICAL CONSTRAINTS OF LAMELLAE FORMING BLOCK COPOLYMERS.

Polymer materials, which can be examined with coarse grained models, should able to capture the physics associated with polymer entanglements. One of possible successful approach relies on using slip springs. However, to inform these coarse grained models of block copolymers, the entanglements should be elucidated. Experiments do not provide the molecular data, so microscopic models are useful tools to study the molecular data. In this work, we study such issue using a Kremer-Grest model as it represents a "microscopic model". This model can be used to obtain the topological constraints of the polymer to inform coarse grained simulations. Defect annihilation of block copolymer nanodomains have been studied recently, and these studies have shown that there is a large kinetic barrier for defect annihilation. These studies has been performed with soft unentangled block copolymers, but in the experimental system, these block copolymers may be entangled. The entanglement effects of block copolymers are studied here using a slip spring model, which was previously developed for homopolymer melts. In this article, a comparison between the soft, slip spring model and a Lennard-Jones polymer is performed. The Lennard-Jones polymer is examined using the Z1 analysis, where it is shown that the topological constraints are increased at the interface of the unlike blocks for shorter chains, but for longer chains the constraints decrease at the interface. For the slip spring model, there is always a decrease of slip springs at the interface; when comparing the two models, we observe that large molecular soft chains mimic the Lennard-Jones polymers in both the topological constraints, but not the orientation of the chains near the interface.

5.1 Introduction

Block copolymers have emerged as a compelling candidate for nanoscale fabrication. The self-assembly of block copolymers can be directed by surface patterns, thereby creating templates for synthesis of organic and inorganic structures such as nanowires [33–35], quantum dots [36, 37], magnetic storage media [38], and silicon capacitors [39]. In the context of lithographic fabrication, attention has focused on the ability to control the self-assembly and orientation of the nanodomains [16]. However, assembling the block copolymers into defect-free structures can be difficult. We know defect-free structures have a low free-energy in equilibrium[40], but defects still occur in experiments[41]. This shows that the defects are occurring due to the kinetics and dynamics of the block copolymers[42, 43]. Recently, Hur *et al.* [44] showed that there are large kinetic barriers for direct self assembly, and chemical patterns reduce this kinetic barrier.

Uneyama and Masubuchi [126] use a Slip-Spring model with many chains that was extended from the Slip-Link model[127], and these simulations reproduced the bead dependence in the transition from the Rouse regime and entangled dynamics. This approach was extended by Langeloth*et al.* [128], but with the DPD thermostat and DPD force field. Recently, Nikoubashman*et al.*[129–131] have used the Theoretically Informed Coarse Grained (TICG) model [26] with slip springs in non equilibrium simulations of cylinder and lamellae forming block copolymers in thin films. The simulations of entangled block copolymers have followed the scaling laws of the tube models, and for non-equilibrium simulations. Similar to previous work, the DPD thermostat where the total number of slip springs fluctuate and a specific chemical potential that is chosen a posteriori.

The soft coarse grained polymers need to reproduce the local physics of real polymer to be applied to the kinetics defect annihilation. The Lennard-Jones polymer model is a great first step for comparing the soft model to a real polymer. There has been a few simulations of block copolymers using the Kremer-Grest model[55], but most have only examined short chains[132]. Murat *et al.*[22], show that in the strong segregation limit the chain stretching lowers the entanglement density. However, recently Sethuraman *et al.* [133] show an increase of the entanglement density using packing arguments by Kavassalis and Noolandi[134]. This analysis was performed with Self-Consistent-Field Theory, Monte Carlo simulations, and the Kremer-Grest model. The analysis was performed for chains of length $N = 100$, while Murat*et al.*[22], explored chains up to $N = 400$ (where there are 85 beads in between the entanglements).

Here, we confirm our TICG simulations are identical to the single-chain theory. A comparison between the soft model and the Kremer-Grest model is performed to ensure the TICG model reproduces the physics of real polymers. The information from these comparisons will allow the model to be used to study the kinetics of defect annihilation.

5.2 Methods and Model

5.2.1 Kremer-Grest Model

We simulated bead spring model with the so-called Kremer-Grest model[55], and we also used the model for symmetric block copolymers[22]. We use this model because the model handles entanglements naturally, so we can capture the topological constraints in the multi-chain model. Following literature[55], we set the parameters, $r_c = 2^{1/6}\sigma_{ij}$, $\epsilon_{AA} = \epsilon_{BB} = \epsilon$, and $\epsilon_{AB}/\epsilon = 1 + \epsilon$, $\sigma_{AA} = \sigma_{BB} = \sigma_{AB} = \sigma$, where the values of $\sigma = \epsilon = k_B T = 1.0$. This produces a density of 0.85. These simulations were initiated with the HOOMD molecular dynamics package, where a simple Gaussian potential, $V_{guass}(r) = \epsilon exp[-0.5(\frac{r}{\sigma})^2]$, with the same parameters as the 12:6 Lennard-Jones potential, but a cut off of $r_c = 3.0$. The simulation next ran the Martyna-Tobia-Klein equations of motion for NPT to orient the chains into lamella for 10 million time steps. After Gaussian relaxation into lamella with the Gaussian potential, the 12:6 LJ potential is turned on and run in the NVE ensemble with a 0.01 limit. After the NVE run, the NPT ensemble is run for 10 million time steps, and then a final 10 million time steps with the Nose-Hoover thermostat. We used $N = 100, 200, 400$

and $\epsilon = 1.5$ and 2.0. For the rest of the article, we will refer to this model as FENE chains.

5.2.2 Theoretically Informed Entangled Polymer Simulation

In this article, we use the Theoretically Informed Entangled Polymer Simulation approach with an implementation of the slip springs (SS) similar to Ramirez *et al.*[23]. Equilibrium and non-equilibrium simulations have been performed with the Theoretically Informed Coarse grained model with block copolymer and homopolymers[23, 24]. The coarse-grained model employed in this work has been described in the literature [16, 25–29, 56, 81]; it takes into account the main characteristics of copolymers, including chain connectivity, compressibility, and the incompatibility of the monomers. Each chain is discretized into N beads; the position of the s^{th} bead on the i^{th} chain in denoted by $\mathbf{r}_i(s)$. The total Hamiltonian can be written as the sum of bonded contributions,H_b and non-bonded contributions,H_{nb}:

$$H(\mathbf{r}_i(s)) = H_b(\mathbf{r}_i(s)) + H_{nb}[\phi_A, \phi_B] \tag{5.1}$$

where $H_b(r_i(s))$ is given by

$$\frac{H_b(r_i(s))}{k_B T} = \frac{3}{2} \sum_{i<j} \left(\frac{r_{ij}}{b}\right)^2 B_{ij} \tag{5.2}$$

and H_{nb} is given by

$$\frac{H_{nb}}{k_B T} = \sqrt{\mathcal{N}} \int\limits_V \frac{dr}{R_e^3} [\chi N \phi_A \phi_B + \frac{\kappa N}{2} (\phi_A + \phi_B)^2] \tag{5.3}$$

the sum in Equation 5.3 runs over all beads (Nn) (where n is the number of chains and N is the number of beads per chain), B_{ij} is either unity if there is a bond linking the beads or zero otherwise, $\phi_K(\mathbf{r})$ is the normalized local density of type A or B beads, V is the volume, and $\sqrt{\mathcal{N}}$ is the number of chains per unit chain volume, which can be extracted from experiments. The interdigitation number is defined by $\sqrt{\mathcal{N}} = \rho_0 R_e^3 / N$ [26], where R_e

is the average end-to-end distance, and $b^2 = R_e^2/(N-1)$, where ρ_0 is the number density of the beads. Essentially, $\overline{\mathcal{N}}$ controls the strength of the fluctuations; it can be estimated from the molecular weight and melt density determined from experiments [78]. The strength of non-bonded interactions between a homopolymer of type A with a homopolymer of type B is determined by the Flory-Huggins parameter,χ, and κ ensures that there is a continuous density throughout the system (a description for the choice of κ is given in Pike *et al.* [25]).

By defining a density cloud $\omega(\mathbf{r})$ around each particle's position, one can compute the beads' local densities ϕ_K. The integral in Equation 5.4 can therefore be written as a sum of pairwise interactions between beads,

$$U_{ij} = \frac{\sqrt{\overline{\mathcal{N}}}}{R_e^3}\left[\kappa N + \chi N(1-\delta_{KK'})\right]\int_V \omega(\mathbf{r}-\mathbf{r_i})\omega(\mathbf{r}-\mathbf{r_j})dr \tag{5.4}$$

where K is either type A or B. The density cloud decays to zero after a cutoff distance r_{int}, which allows for each bead to have a sufficient number of interactions with neighbors, as determined in Detcheverry *et al.* and Pike *et al.* [25, 26]. Spherical step-like functions are used to determine the interactions, so the beads can be thought of as soft spheres where the pair-wise interaction energy is proportional to the overlapping volume of the density clouds. The density clouds are normalized to unity, so $\omega(\mathbf{r}) = C\tilde{\omega}(r)$ where $\tilde{\omega}(r) = 1$ if $r <= r_{int}$, $\tilde{\omega}(r) = 0$ if $r >= r_{int}$, and C is a normalization constant. Following Pike *et al.*, in our simulations each bead interacts on average with 14 beads.

Since TICG uses soft particles, chains are allowed to cross, and the topological constraints (entanglements) are not present. We can use slip-springs to mimic entanglements in the system. The Slip-Links (or springs) are used to capture entanglement dynamics in both single chain and multi-chain model with success. In the multi-chain case the idea is to connect two chain segments on a different chains via elastic potential. This represent topological constraints that chain pose on each other. Slip-Springs are allowed to relax dynamically. The Slip-Springs can slide along the chain backbone, can be destroyed and renewed at the chain ends. There are few Slip-Spring implementations different in details. We follow the approach by Chappa *et al.*[125] and compare the results to the single chain results by Schieber [135].

The slip springs are updated by cycling through each polymer chain, and then cycle through each slip spring and either update or create a slip spring with probability $(\frac{1}{N_{ce}} + \frac{1}{N_{ssc}})$. N_{ce} is the number of chain ends and N_{ssc} is the number of slip springs on the chain. The slip springs can jump to either neighboring beads with a probability of min(1,$exp(-U_{ss}/K_BT)$), where U_{ss} is the potential energy of the slip springs. The springs can be created on the chain ends with a probability min(1,$\xi = exp(\mu/k_BT)$). If a slip spring jumps off of the polymer chain it's destroyed with probability of min(1,$\frac{1}{\xi}$). The slip springs update via Monte Carlo moves, which is the same as previous work [23, 125]. The Slip-Springs do not occupy the same bead which is in accordance to the Slip-Link model[124, 135]. Since the simulations consist of soft block copolymers, there is a density gap near the interface of A and B chains. Here we used the implementation in Chappa *et al.*[125] to ensure we properly account for the density gap. Lastly, when simulating block copolymers, we assume that the slip springs treat each block copolymer block identically. The details of implementation and theory are in Ramirez *et al.* [124].

5.3 Results and Discussion

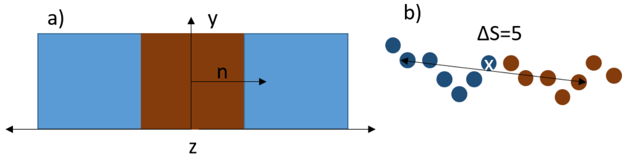

Figure 5.1: a) is the set up of the Kremer-Grest polymers, where n is the vector normal to the interface, and the center of the red lamellae is at z=0. b) is the definition of ΔS for the statistical segment length. A value of $\Delta S = 5$ means the there is a distance of 5 beads from the selected bead.

We prepare the systems in an initial lamellae configuration with the normal in the 'z'

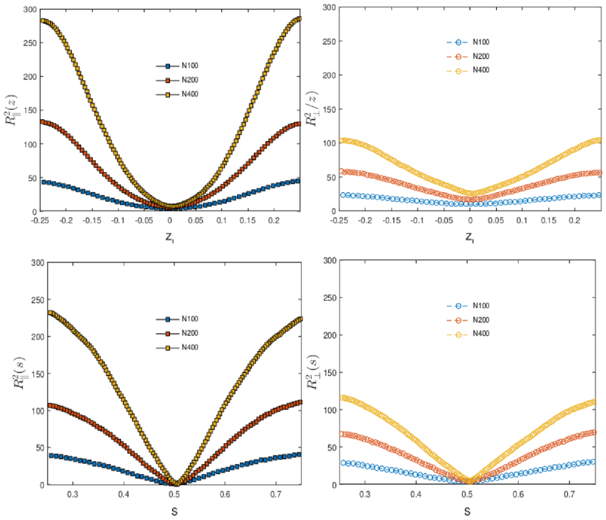

Figure 5.2: Spatial anisotropy of chains and contour position dependent anisotropy of chains. The anisotropy is parallel or perpendicular to the interface. Here, N100 is a FENE polymer with 100 beads per chain of $N = 100$.

direction. The length of the box in the z direction is denoted, L_z and s is the contour of the chain from 0 to 1. The setup can be seen in Figure 5.1 We denote the bead coordinates of the chain as $r^{(i)}_{j=1,N}(t)$ at specific times. We also know the interface normal ($\mathbf{n}$). To resolve the spatial anisotropy of the chains with respect to the interface normal, we use the tensor:

$$\mathbf{R}(z) = \left\langle \mathbf{P}^i_j(t)\mathbf{P}^i_j(t)\delta(\mathbf{n}\mathbf{r}^i_j - z) \right\rangle_{t,i,j} \tag{5.5}$$

where $\mathbf{P}^i_j(t)$ is the secant vector connecting bead j with the center of the chain. The relevant values of $\mathbf{R}$ are the parallel and perpendicular components,

$$R^2_{\parallel} = \mathbf{nn} : \mathbf{R}(z) \tag{5.6}$$

$$R^2_{\perp} = \frac{1}{2}(1 - \mathbf{nn}) : \mathbf{R}(z) \tag{5.7}$$

The results shown in Figure 5.2 show that there is a change in the physical structure of the chains near the interface. The values of $R^2_{\perp}$ (in the direction of n) and $R^2_{\parallel}$ (parallel to n)

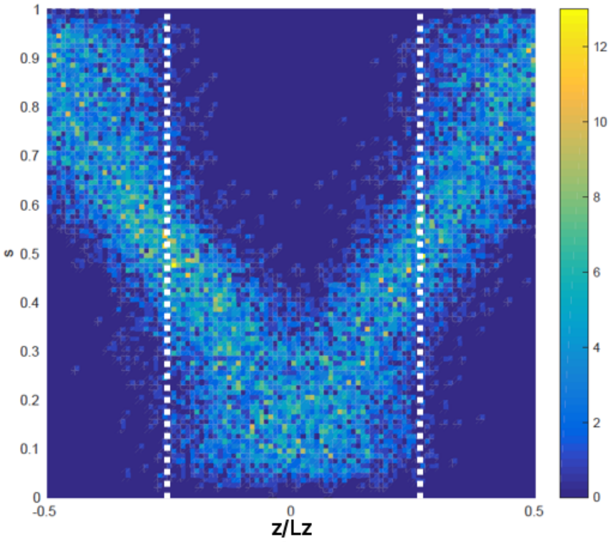

Figure 5.3: A 2D contour plot of the entanglement density for the contour of the chain (s) and through the lamella(L_z) for $N = 100$. The interface is at 0.25 and -0.25 z/Lz. Yellow in the contour map is strongly entangled while blue is weakly entangled.

show there is an anisotropy of the chains parallel and perpendicular to the interface due to the differing slopes near the interface.

The FENE chains were analyzed using the Z1 algorithm[136], through space and contour of the chain. The Z1 algorithm analyzes topological constraints (called kinks), which are where the polymers entangle. In Figure 5.4 and 5.3 shows a contour plot of the entanglements on the contour of the chain and along the lamellae. When the plot is more yellow, there are more entanglements on that specific part of the chain and in space. In Figure 5.5, we show the folded entanglement density through the lamella. For $N = 100$ (Figure 5.3), there is a peak of entanglements at the interface, which is consistent with results in ref [133]. However, when the chains become longer ($N = 400$), the density of entanglements decrease at the interface in Figure 5.5, where the entanglement density was averaged over the contour of the chain. This effect appears because as the chains become longer the chains in the middle of the lamellae are able to entangle more than the $N = 100$ due to the number of entanglements per chain. For $N = 100$, the kinks only exist in the middle of the chain, which happens to be near the interface. The longer chains can entangle at different contours

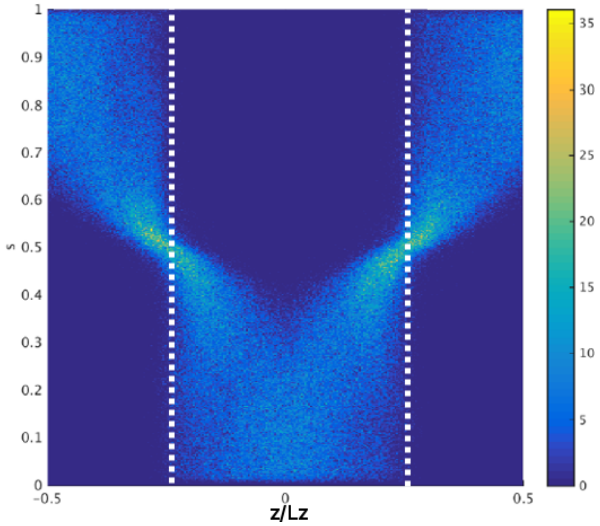

Figure 5.4: A 2D contour plot of the entanglement density for the contour of the chain (s) and through the lamella(L_z) for $N = 400$.The interface is at 0.25 and -0.25 z/Lz (white lines). Yellow in the contour map is strongly entangled while blue is weakly entangled.

of the chain, hence not localized at the interface. This effect is similar to homopolymers near a surface where the number of entanglements is proportional to the density of the monomers[137, 138]. This result can be directly seen in Figures 5.6 and 5.8 when the ratio between the entanglements and the bead number density is plotted in space and contour of the chain. The entanglements causing the local maximum close to the interface are thus close to centers of chains and do not predominantly stem from the dangling ends.

Our model was compared to DSM (Discrete Slip-Link Model) [135]. As seen in Figure 5.9, the multi-chain model gives the same predicted results as DSM for homopolymers. The parameters of the system are $\overline{\mathcal{N}} = 128$, $\kappa N = 50$, $\chi N = 0$, $(\beta_e)_{eff} = 4$, dt=1/100, and time steps before the slip springs are updatedτ_{ss}=100, fraction of A beadsf_A=0.5, N=32. When the simulations are performed with lamellae forming block copolymers ($\chi N = 37$)[26], we see the same predictions as homompolymers. These simulations are for $\xi = 0.015 = exp(\mu/k_BT)$ which can be mapped to an effective chemical potential by $(\beta_e)_{eff}^{-1} = exp(\mu/k_BT) - ln < W(\mu) >= z_{eff}$, which is in correspondence with the analytical predictions by Schieber[135]. The value of ξ corresponds to $(\beta_e)eff = 4$. Here, μ is defined from Chappa*et al.* [125] and

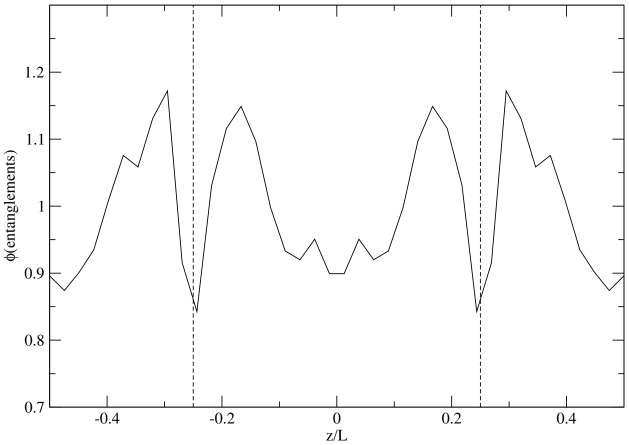

Figure 5.5: The entanglement density through the lamella for $N = 400$. The interface is at 0.25 and -0.25, and z is the z-coordinate normalized by L.

$W = \sum exp(U_{ss}/k_BT)$ where the sum is over all possible empty beads around a specific bead. We vary $(\beta_e)_{eff}$ (Figure 5.10) in our multi-chain simulations, and we see χN has little to no effect when comparing to the single chain theory.

For the soft chains, we perform similar simulations with varying entanglement densities. Here we use two different densities, $\overline{\mathcal{N}} = 58$ and 128. For the $\overline{\mathcal{N}} = 58$, we use the number of slip springs per chain, $< Z > -1 = 5.4$ and 7.1, corresponds to $\xi = 0.009$ and 0.015. For $\overline{\mathcal{N}} = 128$ we use $\xi = 0.009$ or $< Z > -1 = 11.1$. We then plot the density of the slip springs and the monomers for all three cases. This can be seen in Figure 5.11 and 5.12. We then extend the number of beads to $N = 64$ for $\overline{\mathcal{N}} = 128$ and $\xi = 0.009$. The values of $\chi = 1.15$, $\kappa = 1.56$, and $b = \sqrt{1/31}$ were held constant while changing the value of N. Figure 5.13 show the density of the slip springs, and due to the larger χN for $N = 64$ the maximum is larger and the minimum is smaller. In the density of the slip springs for $N = 64$, are much closer to the the densities of the FENE chains in Figure 5.5 ($< Z > -1 = 4.8$).

Instead of changing the molecular weight, as before, we now change the discretization. We use $\overline{\mathcal{N}} = 128$ with $N = 128$ and $N = 64$ ($b = \sqrt{1/N-1}$). As seen in Figure 5.15, the more discretization, the results become closer to the longer FENE chains. At a $N = 128$, we see the results of the entanglement density from the slip spring model closely resemble entanglement density with the FENE chains. Lastly, the ratio of the density of the slip

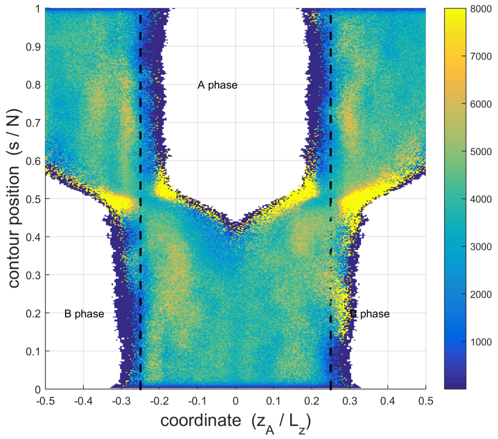

Figure 5.6: The ratio of the entanglement density and the bead number density. Yellow in the contour map is strongly entangled while blue is weakly entangled. The interface is at 0.25 and -0.25.

springs is plotted to the density of the monomers in Figure 5.14. If the ratio was unity, it would imply that the slip springs are not affected by the local density, which is not the case in our simulations[125].

We then measure the local statistical segment length of the chains to observe how the chains orient near the interface. We measure the distance between multiple beads apart, ΔS. The definition of ΔS is shown visually in Figure 5.1, which is the distance of ΔS beads away from the selected bead. This analysis shows the chains orient normal to the interface as seen in Figure 5.16 and 5.17. There is a small dip due the density dip at the interface, and there is an increase in the statistical segment length increases when the beads are about 8σ from the interface. The chains orient normal to the interface due to this increase, and this plot is in qualitative agreement with the entanglement density. The results here shows, in more detail, the same results as Murat*et al.* [22], where the stiffness or orientation normal to the interface is creating the decrease of entanglements.

Since the local statistical segment length is important to the entanglements of the FENE chains, we calculated the packing of the chains in the TICG model. The same analysis for the FENE chains was performed on the TICG model with $N = 32$ and $N = 64$ as seen in Figure 5.18. In Figure 5.18, we see a peak of the local statistical segment length for many

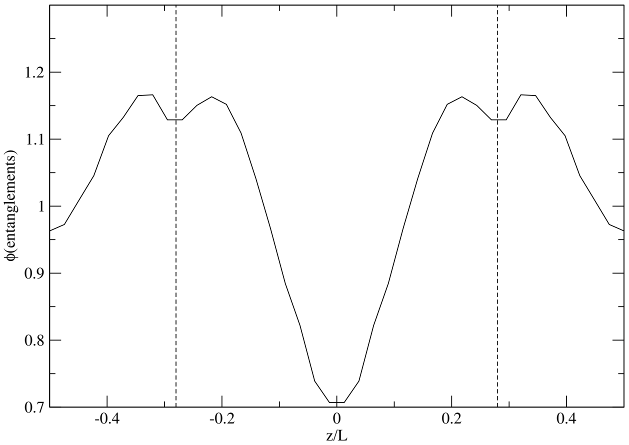

Figure 5.7: The entanglement density through the lamella for $N = 100$. The interface is at -0.25 and 0.25, and z is the z-coordinate normalized by L.

different values of ΔS, which does not occur with the FENE chains. For chains of $N = 64$ and higher, we see the same increase at the interface as the $N = 32$ case.

If we plot the same 2D plot as in Figure 5.3, we obtain Figure 5.19 for $N = 32$. These 2D plots count the number of Slip Springs that jump on to a specific contour of the chain and in space. For the shorter chains, the ends of the chains appear to be entangling more than the middle of the chain (or interface). For the longer chains, the results of $N = 32 and N = 128$ are similar. This effect is due to many slip springs being created and/or destroyed only at the chain ends, which creates more entanglements at the end of the chains. However, Performing and average of the slip springs in space shows there is a decrease of the slip spring density at the interface, and the dip is greater for larger discretization (Figure 5.15).

5.4 Conclusions

Initially, we examined the Kremer-Grest model of block copolymers. We see similar results as ref [133], but show that the entanglement density is not as simple as reported due to the chain orientation near the interface. When exploring longer chain lengths, we found that the chains become oriented normal to the interface and there are less entanglements present in the middle of the chain. We have extended the slip spring model[124] to block copolymers

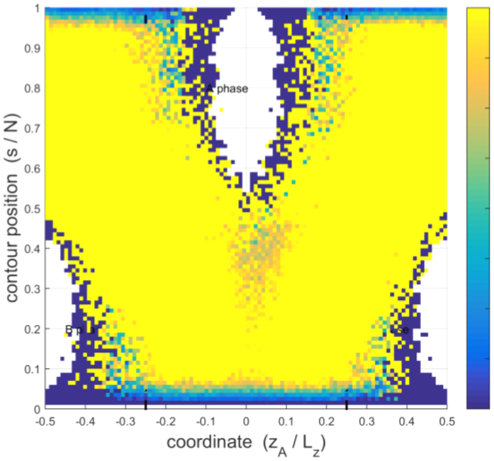

Figure 5.8: The ratio of the entanglement density and the bead number density. Yellow in the contour map is strongly entangled while blue is weakly entangled. The interface is at -0.25 and 0.25.

and found the slip springs follow the single chain model [2] and Chappa *et al.*. [125]. We compared our model to the Kremer-Grest model for block copolymers and measured their entanglement density with the Z1 algorithm. These results are consistent with the soft slip spring model. Since the TICG model is soft and has a low compressibility we do not capture all of the physics of the FENE chains, but we do capture the essential features for longer chains. With the TICG model we will now be able to simulate much longer times for the dynamics and kinetics of entangled block copolymers, specifically in Directed Self Assembly applications.

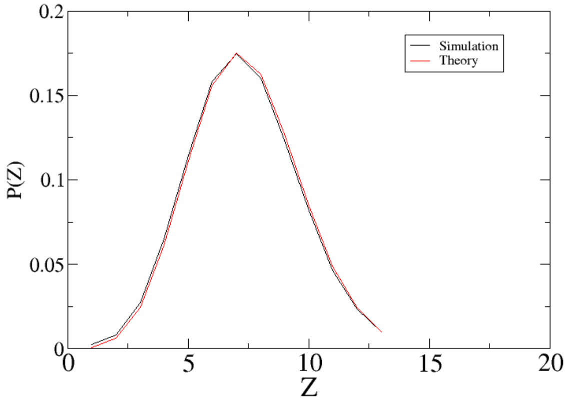

Figure 5.9: The probability of finding and a chain with a specific number of entanglements ($N_{ss} =< Z - 1 >$). The black plot is the TICG simulation and the distribution from single chain theory[2] is the red plot.

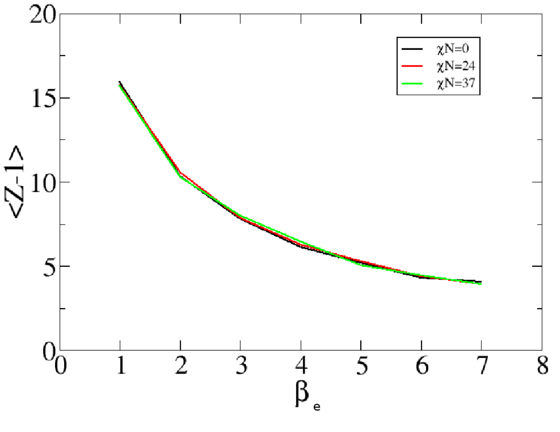

Figure 5.10: The number of slip springs in a simulation ($N_{ss} =< Z - 1 >$) with different values of χN.

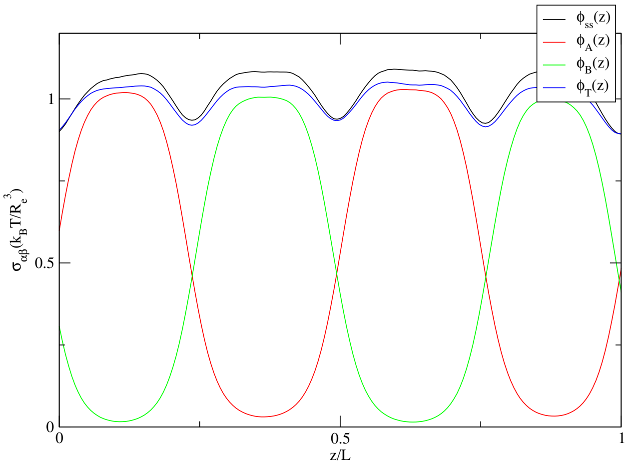

Figure 5.11: Density of slip springs (black), A beads (red), B beads (green), and total monomer density (blue) for $\overline{\mathcal{N}} = 128$, $N = 32$, and $\chi = 37$. The black dashed lines are the interface between the two blocks.

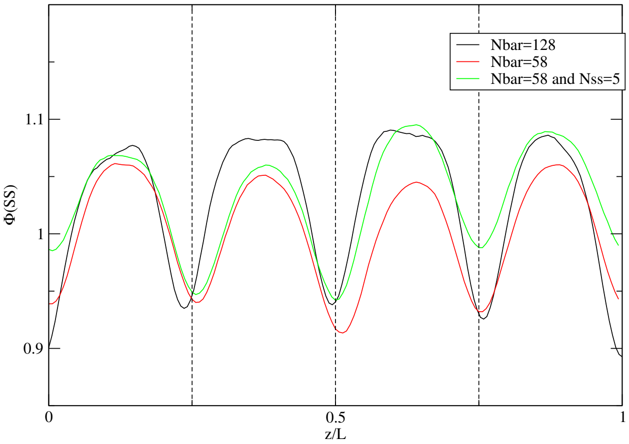

Figure 5.12: Density of slip springs for $\overline{\mathcal{N}} = 128$ (black),$\overline{\mathcal{N}} = 58$ (red), and $\overline{\mathcal{N}} = 58$ (green). Here $N = 32$, and the black dashed lines are the interface between the two blocks.

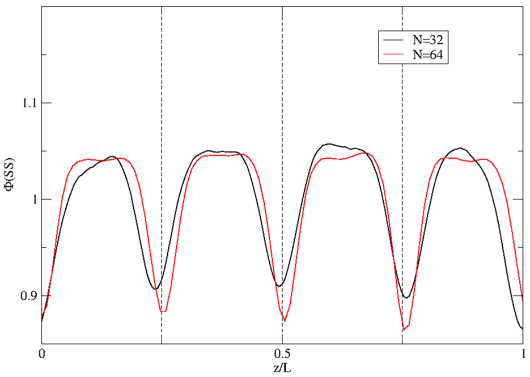

Figure 5.13: Density of slip springs for $\sqrt{\mathcal{N}} = 128$ for $N = 32$ (black) and $N = 64$ (red). Here, $b = \sqrt{(1/31)}$. The black dashed lines are the interface between the two blocks.

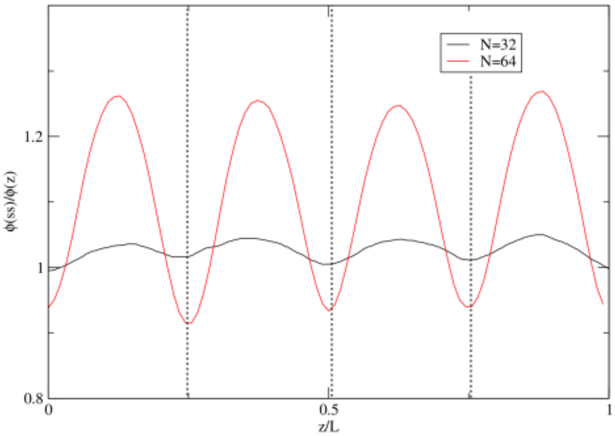

Figure 5.14: The values of $\phi(ss)/\phi(z)$ for $N = 32$ (black) and $N = 64$ (green). Here, $b = \sqrt{(1/31)}$. The black dashed lines are the interface between the two blocks.

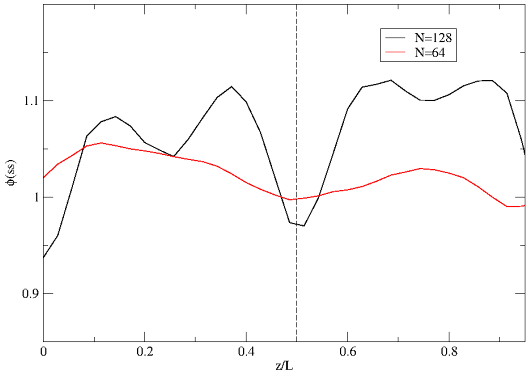

Figure 5.15: The values of $\phi(ss)$ for $N = 128$ (black) and $N = 64$ (red). Here, $b = \sqrt{1/(N-1)}$. The black dashed lines are the interface between the two blocks.

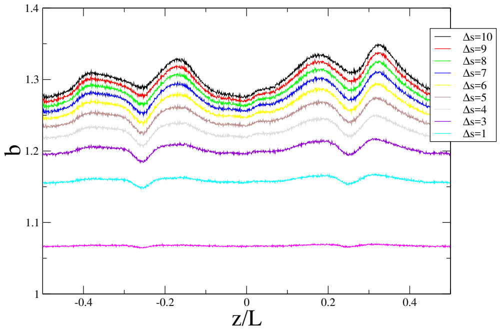

Figure 5.16: The value of the statistical segment length for the FENE chain model. The value of b is calculated from the distances of two beads on a chain that is Δs apart. $N = 400$

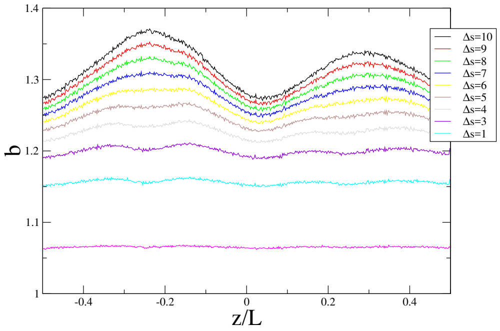

Figure 5.17: The value of the statistical segment length for the FENE chain model. The value of b is calculated from the distances of two beads on a chain that is Δs apart. $N = 100$

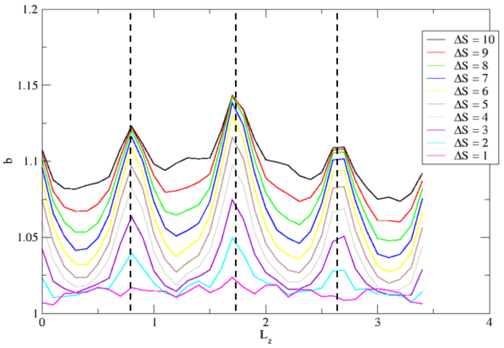

Figure 5.18: The value of the statistical segment length for the TICG. The value of b is calculated from the distances of two beads on a chain that is Δs apart. For $N = 32$, the interfaces are at $L_z = 0, 0.9, 1.8$, and 2.7.

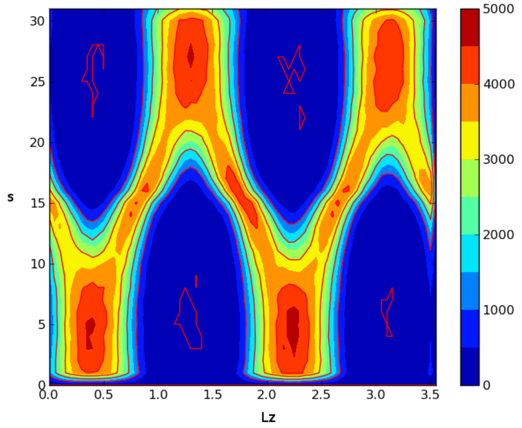

Figure 5.19: Distribution of slip springs in space (z) and on the contour of the chain (s), $N = 32$. The more red in the plots means the polymer is more entangled, and the more blue of the plot the less entangled the polymer is.

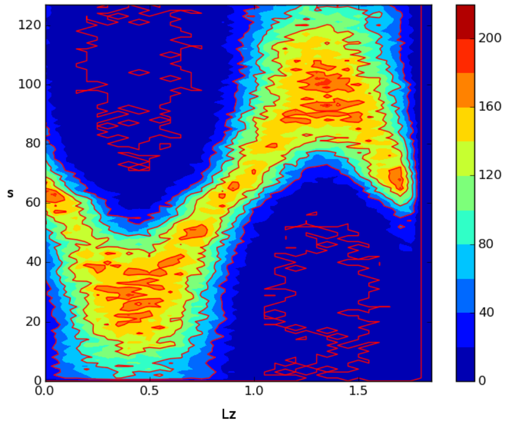

Figure 5.20: Distribution of slip springs in space (z) and on the contour of the chain (s), $N = 128$. The more red in the plots means the polymer is more entangled, and the more blue of the plot the less entangled the polymer is.

CHAPTER 6

CONCLUSIONS AND FUTURE WORK

In this work, the Theoretically Informed Coarse Grained model has shown the ability to predict and reproduce experiments in the so-called Hole-Shrink experiments. The extension of the model to dynamics have shown that it captures both entangled and rouse dynamics. In non-equilibrium simulations the model correctly predicts the phase diagram for lamellae forming block copolymers under shear and predicts the reason the flip in orientations is due to the tumbling motion of specific blocks. When the TICG model included entanglements via slip springs for block copolymers and homopolymers, the model follows the single chain model and the Kremer-Grest model. To ensure our model correctly account for density fluctuations, the Rosenbluth method was implemented for the slip spring model. Using the Rosenbluth method, the slip spring model correctly reproduces the Kremer-Grest model for block copolymers qualitatively.

For the Hole-Shrink experiment the next steps include, PS wetting walls, three dimensional structures that mimic the actual holes in experiments, and more advanced geometries (such as T- or L-shaped holes) will be performed using the knowledge gained in this article to increase the window of the desired structures. Similar work, such as the critical dimensions and displacement of the PMMA holes; homopolymer addition of both PMMA and PS; and SCFT calculations will be analyzed, as in this article. The overfilled case has a large parameter space and should be studied extensively with the addition of three dimensional geometries.

Future work with the slip-spring model should be a study of entangled block copolymers under steady shear examining the lamellar morphologies. The stress and velocity profiles need to be explored as well, as in ref [24]. An implementation of different $(\beta_e)_{eff}$ values for each block also needs to be explored, and this will include a detailed comparison with FENE chains as well. Lastly, once the model has been explored for non equilibrium simulations, the model needs to explore the dynamics and kinetics of Directed Self Assembly of entangled polymers.

REFERENCES

[1] P. Ramachandran and G. Varoquaux, "Mayavi2 user guide," 2008.

[2] J. D. Schieber, "Fluctuations in entanglements of polymer liquids," *The Journal of chemical physics*, vol. 118, no. 11, pp. 5162–5166, 2003.

[3] F. Bates and G. Fredrickson, "Block copolymer thermodynamics: theory and experiment," *Annual Review of Physical Chemistry*, vol. 41, no. 1, pp. 525–557, 1990.

[4] F. Bates and G. Fredrickson, "Block copolymers designer soft materials," *Physics today*, vol. 52, pp. 32–38, 1999.

[5] H. Frielinghaus, N. Hermsdorf, K. Almdal, K. Mortensen, L. Messé, L. Corvazier, J. Fairclough, A. Ryan, P. Olmsted, and I. Hamley, "Micro-vs. macro-phase separation in binary blends of poly (styrene)-poly (isoprene) and poly (isoprene)-poly (ethylene oxide) diblock copolymers," *EPL (Europhysics Letters)*, vol. 53, p. 680, 2001.

[6] D. Angelescu, J. Waller, D. Adamson, P. Deshpande, S. Chou, R. Register, and P. Chaikin, "Macroscopic orientation of block copolymer cylinders in single-layer films by shearing," *Advanced Materials*, vol. 16, no. 19, pp. 1736–1740, 2004.

[7] S. Okamoto, K. Saijo, and T. Hashimoto, "Real-time saxs observations of lamella-forming block copolymers under large oscillatory shear deformation," *Macromolecules*, vol. 27, no. 20, pp. 5547–5555, 1994.

[8] J. Zipfel, P. Lindner, M. Tsianou, P. Alexandridis, and W. Richtering, "Shear-induced formation of multilamellar vesicles (onions) in block copolymers," *Langmuir*, vol. 15, no. 8, pp. 2599–2602, 1999.

[9] G. Arya and A. Panagiotopoulos, "Log-rolling micelles in sheared amphiphilic thin films," *Physical review letters*, vol. 95, no. 18, p. 188301, 2005.

[10] A. Chremos, K. Margaritis, and A. Panagiotopoulos, "Ultra thin films of diblock copolymers under shear," *Soft Matter*, vol. 6, no. 15, pp. 3588–3595, 2010.

[11] G. Arya, J. Rottler, A. Panagiotopoulos, D. Srolovitz, and P. Chaikin, "Shear ordering in thin films of spherical block copolymer," *Langmuir*, vol. 21, no. 24, pp. 11518–11527, 2005.

[12] A. Zvelindovsky, G. Sevink, and J. Fraaije, "Shear-induced transitions in a ternary polymeric system," *Physical Review E*, vol. 62, no. 3, pp. 3063–3066, 2000.

[13] M. Stoykovich, M. Muller, S. Kim, H. Solak, E. Edwards, J. De Pablo, and P. Nealey, "Directed assembly of block copolymer blends into nonregular device-oriented structures," *Science*, vol. 308, no. 5727, pp. 1442–1446, 2005.

[14] M. Stoykovich, H. Kang, K. Daoulas, G. Liu, C. Liu, J. De Pablo, M. Müller, and P. Nealey, "Directed self-assembly of block copolymers for nanolithography: fabrication of isolated features and essential integrated circuit geometries," *Acs Nano*, vol. 1, no. 3, pp. 168–175, 2007.

[15] S. Kim, H. Solak, M. Stoykovich, N. Ferrier, J. de Pablo, and P. Nealey, "Epitaxial self-assembly of block copolymers on lithographically defined nanopatterned substrates," *Nature*, vol. 424, no. 6947, pp. 411–414, 2003.

[16] R. Ruiz, H. Kang, F. Detcheverry, E. Dobisz, D. Kercher, T. Albrecht, J. de Pablo, and P. Nealey, "Density multiplication and improved lithography by directed block copolymer assembly," *Science*, vol. 321, no. 5891, pp. 936–939, 2008.

[17] A. Marencic and R. Register, "Controlling Order in Block Copolymer Thin Films for Nanopatterning Applications," *Annual Review of Chemical and Biomolecular Engineering*, vol. 1, pp. 277–297, 2010.

[18] R. Segalman, "Patterning with block copolymer thin films," *Materials Science and Engineering: R: Reports*, vol. 48, no. 6, pp. 191–226, 2005.

[19] M. Matsen, "The standard Gaussian model for block copolymer melts," *Journal of Physics: Condensed Matter*, vol. 14, pp. R21–R47, 2002.

[20] M. Matsen, "Thin films of block copolymer," *The Journal of chemical physics*, vol. 106, no. 18, pp. 7781–7791, 1997.

[21] G. Fredrickson, *The equilibrium theory of inhomogeneous polymers*, vol. 134. Oxford University Press, 2005.

[22] M. Murat, G. S. Grest, and K. Kremer, "Statics and dynamics of symmetric diblock copolymers: A molecular dynamics study," *Macromolecules*, vol. 32, no. 3, pp. 595–609, 1999.

[23] A. Ramírez-Hernández, F. A. Detcheverry, B. L. Peters, V. C. Chappa, K. S. Schweizer, M. Muller, and J. J. de Pablo, "Dynamical simulations of coarse grain polymeric systems: Rouse and entangled dynamics," *Macromolecules*, vol. 46, no. 15, pp. 6287–6299, 2013.

[24] B. L. Peters, A. Ramírez-Hernández, D. Q. Pike, M. Müller, and J. J. de Pablo, "Nonequilibrium simulations of lamellae forming block copolymers under steady shear: A comparison of dissipative particle dynamics and brownian dynamics," *Macromolecules*, vol. 45, no. 19, pp. 8109–8116, 2012.

[25] D. Pike, F. Detcheverry, M. Müller, and J. de Pablo, "Theoretically informed coarse grain simulations of polymeric systems," *The Journal of chemical physics*, vol. 131, p. 084903, 2009.

[26] F. Detcheverry, H. Kang, K. Daoulas, M. Müller, P. Nealey, and J. de Pablo, "Monte Carlo simulations of a coarse grain model for block copolymers and nanocomposites," *Macromolecules*, vol. 41, no. 13, pp. 4989–5001, 2008.

[27] F. Detcheverry, D. Pike, U. Nagpal, P. Nealey, and J. Pablo, "Theoretically informed coarse grain simulations of block copolymer melts: method and applications," *Soft Matter*, vol. 5, no. 24, pp. 4858–4865, 2009.

[28] U. Nagpal, F. Detcheverry, P. Nealey, and J. de Pablo, "Morphologies of linear triblock copolymers from monte carlo simulations," *Macromolecules*, vol. 44, no. 13, pp. 3444–3459, 2011.

[29] F. Detcheverry, P. Nealey, and J. de Pablo, "Directed assembly of a cylinder-forming diblock copolymer: Topographic and chemical patterns," *Macromolecules*, vol. 43, no. 15, pp. 6495–6504, 2010.

[30] H. Guo, K. Kremer, and T. Soddemann, "Nonequilibrium molecular dynamics simulation of shear-induced alignment of amphiphilic model systems," *Physical Review E*, vol. 66, no. 6, p. 061503, 2002.

[31] H. Guo, "Shear-induced parallel-to-perpendicular orientation transition in the amphiphilic lamellar phase: A nonequilibrium molecular-dynamics simulation study," *The Journal of chemical physics*, vol. 124, p. 054902, 2006.

[32] W. Liu, H. Qian, Z. Lu, Z. Li, and C. Sun, "Dissipative particle dynamics study on the morphology changes of diblock copolymer lamellar microdomains due to steady shear," *Physical Review E*, vol. 74, no. 2, p. 021802, 2006.

[33] T. Thurn-Albrecht, J. Schotter, G. Kastle, N. Emley, T. Shibauchi, L. Krusin-Elbaum, K. Guarini, C. Black, M. Tuominen, and T. Russell, "Ultrahigh-density nanowire arrays grown in self-assembled diblock copolymer templates," *Science*, vol. 290, no. 5499, pp. 2126–2129, 2000.

[34] H. Kim, X. Jia, C. Stafford, D. Kim, T. McCarthy, M. Tuominen, C. Hawker, and T. Russell, "A route to nanoscopic SiO_2 posts via block copolymer templates," *Advanced Materials*, vol. 13, no. 11, pp. 795–797, 2001.

[35] W. Lopes and H. Jaeger, "Hierarchical self-assembly of metal nanostructures on diblock copolymer scaffolds," *Nature*, vol. 414, no. 6865, pp. 735–738, 2001.

[36] M. Park, C. Harrison, P. Chaikin, R. Register, and D. Adamson, "Block Copolymer Lithography: Periodic Arrays of ~10^{11} Holes in 1 Square Centimeter," *Science*, vol. 276, no. 5317, pp. 1401–1404, 1997.

[37] R. Li, P. Dapkus, M. Thompson, W. Jeong, C. Harrison, P. Chaikin, R. Register, and D. Adamson, "Dense arrays of ordered GaAs nanostructures by selective area growth on substrates patterned by block copolymer lithography," *Applied Physics Letters*, vol. 76, pp. 1689–1691, 2000.

[38] J. Cheng, C. Ross, V. Chan, E. Thomas, R. Lammertink, and G. Vancso, “Formation of a cobalt magnetic dot array via block copolymer lithography,” *Advanced Materials*, vol. 13, no. 15, pp. 1174–1178, 2001.

[39] C. Black, K. Guarini, K. Milkove, S. Baker, T. Russell, and M. Tuominen, “Integration of self-assembled diblock copolymers for semiconductor capacitor fabrication,” *Applied Physics Letters*, vol. 79, p. 409, 2001.

[40] U. Nagpal, M. Muller, P. F. Nealey, and J. J. de Pablo, “Free energy of defects in ordered assemblies of block copolymer domains,” *ACS Macro Letters*, vol. 1, no. 3, pp. 418–422, 2012.

[41] P. R. Delgadillo, R. Harukawa, M. Suri, S. Durant, A. Cross, V. R. Nagaswami, D. Van Den Heuvel, R. Gronheid, and P. Nealey, “Defect source analysis of directed self-assembly process (dsa of dsa),” in *SPIE Advanced Lithography*, pp. 86800L–86800L, International Society for Optics and Photonics, 2013.

[42] E. Edwards, M. Stoykovich, M. Müller, H. Solak, J. De Pablo, and P. Nealey, “Mechanism and kinetics of ordering in diblock copolymer thin films on chemically nanopatterned substrates,” *Journal of Polymer Science Part B: Polymer Physics*, vol. 43, no. 23, pp. 3444–3459, 2005.

[43] W. Li, P. F. Nealey, J. J. de Pablo, and M. Müller, “Defect removal in the course of directed self-assembly is facilitated in the vicinity of the order-disorder transition,” *Physical review letters*, vol. 113, no. 16, p. 168301, 2014.

[44] S.-M. Hur, V. Thapar, A. Ramírez-Hernández, G. Khaira, T. Segal-Peretz, P. A. Rincon-Delgadillo, W. Li, M. Müller, P. F. Nealey, and J. J. de Pablo, “Molecular pathways for defect annihilation in directed self-assembly,” *Proceedings of the National Academy of Sciences*, vol. 112, no. 46, pp. 14144–14149, 2015.

[45] Y. Seino, H. Yonemitsu, H. Sato, K. Masahiro, and K. Hikazu, “Contact hole shrink process using directed self-assembly,” *Proc. of SPIE Vol*, vol. 8323, pp. 83230–83230, 2012.

[46] H. Yi, X. Bao, J. Zhang, R. Tiberio, J. Conway, L. Chang, S. Mitra, and H. Wong, “Contact-hole patterning for random logic circuits using block copolymer directed self-assembly,” *Proc. of SPIE Vol*, vol. 8323, pp. 83230W–83230W, 2012.

[47] H. Yi, X.-Y. Bao, J. Zhang, C. Bencher, L.-W. Chang, X. Chen, R. Tiberio, J. Conway, H. Dai, and Y. Chen, “Flexible control of block copolymer directed self-assembly using small, topographical templates: Potential lithography solution for integrated circuit contact hole patterning,” *Advanced Materials*, vol. 24, no. 23, pp. 3107–3114, 2012.

[48] M. Somervell, R. Gronheid, J. Hooge, K. Nafus, P. Delgadillo, C. Thode, T. Younkin, K. Matsunaga, B. Rathsack, and S. Scheer, “Comparison of directed self-assembly integrations,” *Proc. of SPIE Vol*, vol. 8325, pp. 83250G–83250G, 2012.

[49] F. Yamashita, E. Nishimura, K. Yatsuda, H. Mochiki, and J. Bannister, “Exploration of suitable dry etch technologies for directed self-assembly,” *Proc. of SPIE Vol*, vol. 8328, pp. 83280T–83280T, 2012.

[50] B. Rathsack, M. Somervell, J. Hooge, M. Muramatsu, K. Tanouchi, T. Kitano, E. Nishimura, K. Yatsuda, S. Nagahara, and I. Hiroyuki, “Pattern scaling with directed self assembly through lithography and etch process integration,” *SPIE Advanced Lithography*, pp. 83230B–83230B, 2012.

[51] A. Lees and S. Edwards, “The computer study of transport processes under extreme conditions,” *Journal of Physics C: Solid State Physics*, vol. 5, p. 1921, 1972.

[52] M. W. Hamersky, M. Tirrell, and T. P. Lodge, “Anisotropy of diffusion in a lamellar styrene-isoprene block copolymer,” *Langmuir*, vol. 14, no. 24, pp. 6974–6979, 1998.

[53] M. Dalvi, C. Eastman, and T. Lodge, “Diffusion in microstructured block copolymers: Chain localization and entanglements,” *Physical review letters*, vol. 71, no. 16, p. 2591, 1993.

[54] M. Müller and J. J. de Pablo, “Computational approaches for the dynamics of structure formation in self-assembling polymeric materials,” *Annual Review of Materials Research*, vol. 43, pp. 1–34, 2013.

[55] K. Kremer and G. S. Grest, “Dynamics of entangled linear polymer melts: A molecular-dynamics simulation,” *The Journal of Chemical Physics*, vol. 92, no. 8, pp. 5057–5086, 1990.

[56] G. Liu, A. Ramírez-Hernández, H. Yoshida, K. Nygård, D. Satapathy, O. Bunk, J. de Pablo, and P. Nealey, “Morphology of lamellae-forming block copolymer films between two orthogonal chemically nanopatterned striped surface,” *Physical Review Letters*, vol. 108, no. 6, p. 065502, 2012.

[57] J.-B. Chang, J. G. Son, A. F. Hannon, A. Alexander-Katz, C. A. Ross, and K. K. Berggren, “Aligned sub-10-nm block copolymer patterns templated by post arrays,” *ACS nano*, vol. 6, no. 3, pp. 2071–2077, 2012.

[58] A. T. KG, K. Gotrik, A. Hannon, A. Alexander-Katz, C. Ross, and K. Berggren, “Templating three-dimensional self-assembled structures in bilayer block copolymer films,” *Science*, vol. 336, no. 6086, pp. 1294–1298, 2012.

[59] R. Segalman, H. Yokoyama, and E. Kramer, “Graphoepitaxy of spherical domain block copolymer films,” *Advanced Materials*, vol. 13, no. 15, pp. 1152–1155, 2001.

[60] R. Segalman, A. Hexemer, and E. Kramer, “Edge effects on the order and freezing of a 2d array of block copolymer spheres,” *Physical review letters*, vol. 91, no. 19, p. 196101, 2003.

[61] R. Segalman, A. Hexemer, and E. Kramer, “Effects of lateral confinement on order in spherical domain block copolymer thin films,” *Macromolecules*, vol. 36, no. 18, pp. 6831–6839, 2003.

[62] R. Segalman, K. Schaefer, G. Fredrickson, E. Kramer, and S. Magonov, “Topographic templating of islands and holes in highly asymmetric block copolymer films,” *Macromolecules*, vol. 36, no. 12, pp. 4498–4506, 2003.

[63] J. Cheng, C. Ross, E. Thomas, H. Smith, and G. Vancso, “Fabrication of nanostructures with long-range order using block copolymer lithography,” *Applied physics letters*, vol. 81, no. 19, pp. 3657–3659, 2002.

[64] J. Cheng, A. Mayes, and C. Ross, “Nanostructure engineering by templated self-assembly of block copolymers,” *Nature materials*, vol. 3, no. 11, pp. 823–828, 2004.

[65] J. Cheng, C. Ross, E. Thomas, H. Smith, and G. Vancso, “Templated self-assembly of block copolymers: Effect of substrate topography,” *Advanced Materials*, vol. 15, no. 19, pp. 1599–1602, 2003.

[66] D. Sundrani, S. Darling, and S. Sibener, “Guiding polymers to perfection: macroscopic alignment of nanoscale domains,” *Nano Letters*, vol. 4, no. 2, pp. 273–276, 2004.

[67] D. Sundrani, S. Darling, and S. Sibener, “Hierarchical assembly and compliance of aligned nanoscale polymer cylinders in confinement,” *Langmuir*, vol. 20, no. 12, pp. 5091–5099, 2004.

[68] M. Hammond and E. Kramer, “Edge effects on thermal disorder in laterally confined diblock copolymer cylinder monolayers,” *Macromolecules*, vol. 39, no. 4, pp. 1538–1544, 2006.

[69] M. Hammond, E. Cochran, G. Fredrickson, and E. Kramer, “Temperature dependence of order, disorder, and defects in laterally confined diblock copolymer cylinder monolayers,” *Macromolecules*, vol. 38, no. 15, pp. 6575–6585, 2005.

[70] S. Park, M. Stoykovich, R. Ruiz, Y. Zhang, C. Black, and P. Nealey, “Directed assembly of lamellae-forming block copolymers by using chemically and topographically patterned substrates,” *Advanced Materials*, vol. 19, no. 4, pp. 607–611, 2007.

[71] K. Shin, H. Xiang, S. Moon, T. Kim, T. McCarthy, and T. Russell, “Curving and frustrating flatland,” *Science*, vol. 306, no. 5693, pp. 76–76, 2004.

[72] H. Takahashi, N. Laachi, K. Delaney, S. Hur, C. Weinheimer, D. Shykind, and G. Fredrickson, “Defectivity in laterally confined lamella-forming diblock copolymers: Thermodynamic and kinetic aspects,” *Macromolecules*, vol. 45, no. 15, pp. 6253–6265.

[73] S. Hur, C. Garcia-Cervera, E. Kramer, and G. Fredrickson, “Scft simulations of thin film blends of block copolymer and homopolymer laterally confined in a square well,” *Macromolecules*, vol. 42, no. 15, pp. 5861–5872, 2009.

[74] K. Stuen, F. Detcheverry, G. Craig, C. Thomas, R. Farrell, M. Morris, J. de Pablo, and P. Nealey, "Graphoepitaxial assembly of asymmetric ternary blends of block copolymers and homopolymers," *Nanotechnology*, vol. 21, no. 49, p. 495301, 2010.

[75] S. Kim, D. O. Shin, D.-G. Choi, J.-R. Jeong, J. H. Mun, Y.-B. Yang, J. U. Kim, S. O. Kim, and J.-H. Jeong, "Graphoepitaxy of block-copolymer self-assembly integrated with single-step zno nanoimprinting," *Small*, vol. 8, no. 10, pp. 1563–1569, 2012.

[76] A. Bosse, C. García-Cervera, and G. Fredrickson, "Microdomain ordering in laterally confined block copolymer thin films," *Macromolecules*, vol. 40, no. 26, pp. 9570–9581, 2007.

[77] E. Helfand, "Block copolymer theory. III. Statistical mechanics of the microdomain structure," *Macromolecules*, vol. 8, no. 4, pp. 552–556, 1975.

[78] K. Daoulas, M. Müller, J. Pablo, P. Nealey, and G. Smith, "Morphology of multi-component polymer systems: single chain in mean field simulation studies," *Soft Matter*, vol. 2, no. 7, pp. 573–583, 2006.

[79] D. Q. Pike, M. Müller, and J. J. de Pablo, "Monte-carlo simulation of ternary blends of block copolymers and homopolymers," *The Journal of chemical physics*, vol. 135, p. 114904, 2011.

[80] A. Ramírez-Hernández, M. Müller, and J. J. de Pablo, "Theoretically informed entangled polymer simulations: linear and non-linear rheology of melts," *Soft Matter*, vol. 9, no. 6, pp. 2030–2036, 2013.

[81] G. Liu, F. Detcheverry, A. Ramírez-Hernández, H. Yoshida, Y. Tada, J. de Pablo, and P. Nealey, "Nonbulk complex structures in thin films of symmetric block copolymers on chemically nanopatterned surfaces," *Macromolecules*, vol. 45, no. 9, pp. 3986–3992, 2012.

[82] A. Ramírez-Hernández, G. Liu, P. Nealey, and J. de Pablo, "Symmetric diblock copolymers confined by two nanopatterned surfaces," *Macromolecules*, 2012.

[83] J. Baschnagel, J. P. Wittmer, and H. Meyer, "Monte carlo simulation of polymers: coarse-grained models," *arXiv preprint cond-mat/0407717*, 2004.

[84] N. Laachi, K. T. Delaney, B. Kim, S.-M. Hur, R. Bristol, D. Shykind, C. J. Weinheimer, and G. H. Fredrickson, "Self-consistent field theory investigation of directed self-assembly in cylindrical confinement," *Journal of Polymer Science Part B: Polymer Physics*, 2014.

[85] C. Bencher, H. Yi, J. Zhou, M. Cai, J. Smith, L. Miao, O. Montal, S. Blitshtein, A. Lavi, and K. Dotan, "Directed self-assembly defectivity assessment. part ii," *SPIE Advanced Lithography*, pp. 83230N–83230N, 2012.

[86] A. Latypov, M. Preil, G. Schmid, J. Xu, H. Yi, K. Yoshimoto, and Y. Zou, "Exploration of the directed self-assembly based nano-fabrication design space using computational simulations," *Proc. SPIE*, vol. 8680, pp. 868013–868023, 2013.

[87] T. Iwama, N. Laachi, K. T. Delaney, B. Kim, S.-M. Hur, R. Bristol, D. Shykind, C. J. Weinheimer, and G. H. Fredrickson, "The hole shrink problem: Directed self-assembly using self-consistent field theory," *Journal of Photopolymer Science and Technology*, vol. 26, no. 1, pp. 15–20, 2013.

[88] N. Laachi, K. T. Delaney, B. Kim, S.-M. Hur, R. Bristol, D. Shykind, C. J. Weinheimer, and G. H. Fredrickson, "The hole shrink problem: Theoretical studies of directed self-assembly in cylindrical confinement," *SPIE Advanced Lithography*, pp. 868014–868014, 2013.

[89] B. Kim, N. Laachi, and G. H. Fredrickson, "Defectivity study of directed self-assembly of cylindrical diblock copolymers in laterally confined thin channels," *SPIE Advanced Lithography*, pp. 868016–868016, 2013.

[90] N. Laachi, T. Iwama, K. T. Delaney, B. Kim, R. Bristol, D. Shykind, C. J. Weinheimer, and G. H. Fredrickson, "Field-theoretic simulations of directed self-assembly in cylindrical confinement: placement and rectification aspects," *SPIE Advanced Lithography*, pp. 90491M–90491M, 2014.

[91] B. Kim, N. Laachi, K. T. Delaney, and G. H. Fredrickson, "Directed self-assembly of diblock copolymers in laterally confining channels: Effect of rough surfaces on line-edge roughness (ler) and defectivity," *SPIE Advanced Lithography*, pp. 90491D–90491D, 2014.

[92] T. Iwama, N. Laachi, K. T. Delaney, B. Kim, and G. H. Fredrickson, "Computational studies of shape rectification in directed self-assembly," *SPIE Advanced Lithography*, pp. 904927–904927, 2014.

[93] K. Fukawatase, K. Yoshimoto, M. Ohshima, Y. Naka, S. Maeda, S. Tanaka, S. Morita, H. Aoyama, and S. Mimotogi, "Dfm for defect-free dsa hole shrink process," *SPIE Advanced Lithography*, pp. 90491K–90491K, 2014.

[94] K. Koppi, M. Tirrell, and F. Bates, "Shear-induced isotropic-to-lamellar transition," *Physical review letters*, vol. 70, no. 10, pp. 1449–1452, 1993.

[95] K. Koppi, M. Tirrell, F. Bates, K. Almdal, and R. Colby, "Lamellae orientation in dynamically sheared diblock copolymer melts," *Journal de Physique II*, vol. 2, no. 11, pp. 1941–1959, 1992.

[96] S. Patel, R. Larson, K. Winey, and H. Watanabe, "Shear orientation and rheology of a lamellar polystyrene-polyisoprene block copolymer," *Macromolecules*, vol. 28, no. 12, pp. 4313–4318, 1995.

[97] B. Riise, G. Fredrickson, R. Larson, and D. Pearson, "Rheology and shear-induced alignment of lamellar diblock and triblock copolymers," *Macromolecules*, vol. 28, no. 23, pp. 7653–7659, 1995.

[98] V. Gupta, R. Krishnamoorti, J. Kornfield, and S. Smith, "Evolution of microstructure during shear alignment in a polystyrene-polyisoprene lamellar diblock copolymer," *Macromolecules*, vol. 28, no. 13, pp. 4464–4474, 1995.

[99] H. Leist, D. Maring, T. Thurn-Albrecht, and U. Wiesner, "Double flip of orientation for a lamellar diblock copolymer under shear," *The Journal of chemical physics*, vol. 110, p. 8225, 1999.

[100] G. Fredrickson, "Steady shear alignment of block copolymers near the isotropic-lamellar transition," *Journal of Rheology*, vol. 38, no. 4, pp. 1045–1068, 1994.

[101] I. Rychkov, "Block copolymers under shear flow," *Macromolecular theory and simulations*, vol. 14, no. 4, pp. 207–242, 2005.

[102] Z. Chen and J. Kornfield, "Flow-induced alignment of lamellar block copolymer melts," *Polymer*, vol. 39, no. 19, pp. 4679–4699, 1998.

[103] I. Hamley, "The effect of shear on ordered block copolymer solutions," *Current opinion in colloid & interface science*, vol. 5, no. 5-6, pp. 341–349, 2000.

[104] J. Cui, Z. Ma, W. Li, and W. Jiang, "Self-assembly of diblock copolymers under shear flow: A simulation study by combining the self-consistent field and lattice boltzmann method," *Chemical Physics*, 2011.

[105] R. Groot, T. Madden, and D. Tildesley, "On the role of hydrodynamic interactions in block copolymer microphase separation," *The Journal of Chemical Physics*, vol. 110, p. 9739, 1999.

[106] R. Groot and T. Madden, "Dynamic simulation of diblock copolymer microphase separation," *The Journal of Chemical Physics*, vol. 108, p. 8713, 1998.

[107] R. Groot and P. Warren, "Dissipative particle dynamics: Bridging the gap between atomistic and mesoscopic simulation," *Journal of Chemical Physics*, vol. 107, no. 11, p. 4423, 1997.

[108] B. Fraser, C. Denniston, and M. Müser, "On the orientation of lamellar block copolymer phases under shear," *The Journal of chemical physics*, vol. 124, p. 104902, 2006.

[109] M. Lísal and J. Brennan, "Alignment of lamellar diblock copolymer phases under shear: Insight from dissipative particle dynamics simulations," *Langmuir*, vol. 23, no. 9, pp. 4809–4818, 2007.

[110] E. Edwards, M. Müller, M. Stoykovich, H. Solak, J. de Pablo, and P. Nealey, "Dimensions and shapes of block copolymer domains assembled on lithographically defined chemically patterned substrates," *Macromolecules*, vol. 40, no. 1, pp. 90–96, 2007.

[111] F. Detcheverry, G. Liu, P. Nealey, and J. de Pablo, “Interpolation in the directed assembly of block copolymers on nanopatterned substrates: Simulation and experiments,” *Macromolecules*, vol. 43, no. 7, pp. 3446–3454, 2010.

[112] A. Abelardo Ramírez-Hernández, F. Detcheverry, B. Peters, and J. J. de Pablo, “In prepartion,”

[113] C. Pastorino, T. Kreer, M. Müller, and K. Binder, “Comparison of dissipative particle dynamics and langevin thermostats for out-of-equilibrium simulations of polymeric systems,” *Physical Review E*, vol. 76, no. 2, p. 026706, 2007.

[114] P. Espanol and P. Warren, “Statistical mechanics of dissipative particle dynamics,” *EPL (Europhysics Letters)*, vol. 30, p. 191, 1995.

[115] P. Hoogerbrugge and J. Koelman, “Simulating microscopic hydrodynamic phenomena with dissipative particle dynamics,” *EPL (Europhysics Letters)*, vol. 19, p. 155, 1992.

[116] F. Müller-Plathe, “Reversing the perturbation in nonequilibrium molecular dynamics: An easy way to calculate the shear viscosity of fluids,” *Physical Review E*, vol. 59, no. 5, p. 4894, 1999.

[117] A. Khandpur, S. Foerster, F. Bates, I. Hamley, A. Ryan, W. Bras, K. Almdal, and K. Mortensen, “Polyisoprene-polystyrene diblock copolymer phase diagram near the order-disorder transition,” *Macromolecules*, vol. 28, no. 26, pp. 8796–8806, 1995.

[118] F. Varnik, J. Baschnagel, and K. Binder, “Molecular dynamics results on the pressure tensor of polymer films,” *The Journal of Chemical Physics*, vol. 113, p. 4444, 2000.

[119] P. Maniadis, T. Lookman, E. Kober, and K. Rasmussen, “Stress distributions in diblock copolymers,” *Physical review letters*, vol. 99, no. 4, p. 48302, 2007.

[120] M. Doi and S. Edwards, *The theory of polymer dynamics*, vol. 73. Oxford University Press, USA, 1988.

[121] P. De Gennes, *Scaling concepts in polymer physics.* Cornell Univ Pr, 1979.

[122] T. Kreer, M. Müser, K. Binder, and J. Klein, “Frictional drag mechanisms between polymer-bearing surfaces,” *Langmuir*, vol. 17, no. 25, pp. 7804–7813, 2001.

[123] H. Noguchi and G. Gompper, “Transport coefficients of off-lattice mesoscale-hydrodynamics simulation techniques,” *Physical Review E*, vol. 78, no. 1, p. 016706, 2008.

[124] Ramírez-Hernández, B. Peters, M. Andreev, J. Schieber, and J. de Pablo, “A multichain polymer slip-spring model with fluctuating number of entanglements for linear and nonlinear rheology,” *The Journal of chemical physics*, submitted 2015.

[125] V. C. Chappa, D. C. Morse, A. Zippelius, and M. Müller, “Translationally invariant slip-spring model for entangled polymer dynamics,” *Physical review letters*, vol. 109, no. 14, p. 148302, 2012.

[126] T. Uneyama and Y. Masubuchi, "Multi-chain slip-spring model for entangled polymer dynamics," *The Journal of chemical physics*, vol. 137, no. 15, p. 154902, 2012.

[127] A. E. Likhtman, "Single-chain slip-link model of entangled polymers: Simultaneous description of neutron spin-echo, rheology, and diffusion," *Macromolecules*, vol. 38, no. 14, pp. 6128–6139, 2005.

[128] M. Langeloth, Y. Masubuchi, M. C. Böhm, and F. Müller-Plathe, "Recovering the reptation dynamics of polymer melts in dissipative particle dynamics simulations via slip-springs," *The Journal of chemical physics*, vol. 138, no. 10, p. 104907, 2013.

[129] A. Nikoubashman, R. L. Davis, B. T. Michal, P. M. Chaikin, R. A. Register, and A. Z. Panagiotopoulos, "Thin films of homopolymers and cylinder-forming diblock copolymers under shear," *ACS nano*, vol. 8, no. 8, pp. 8015–8026, 2014.

[130] A. Nikoubashman, R. A. Register, and A. Z. Panagiotopoulos, "Simulations of shear-induced morphological transitions in block copolymers," *Soft Matter*, vol. 9, no. 42, pp. 9960–9971, 2013.

[131] A. Nikoubashman, R. A. Register, and A. Z. Panagiotopoulos, "Sequential domain realignment driven by conformational asymmetry in block copolymer thin films," *Macromolecules*, vol. 47, no. 3, pp. 1193–1198, 2014.

[132] M. A. Horsch, Z. Zhang, C. R. Iacovella, and S. C. Glotzer, "Hydrodynamics and microphase ordering in block copolymers: Are hydrodynamics required for ordered phases with periodicity in more than one dimension?," *The Journal of chemical physics*, vol. 121, no. 22, pp. 11455–11462, 2004.

[133] V. Sethuraman, D. Kipp, and V. Ganesan, "Entanglements in lamellar phases of diblock copolymers," *Macromolecules*, vol. 48, no. 17, pp. 6321–6328, 2015.

[134] T. A. Kavassalis and J. Noolandi, "A new theory of entanglements and dynamics in dense polymer systems," *Macromolecules*, vol. 21, no. 9, pp. 2869–2879, 1988.

[135] J. D. Schieber and M. Andreev, "Entangled polymer dynamics in equilibrium and flow modeled through slip links," *Annual review of chemical and biomolecular engineering*, vol. 5, pp. 367–381, 2014.

[136] M. Kröger, "Shortest multiple disconnected path for the analysis of entanglements in two-and three-dimensional polymeric systems," *Computer Physics Communications*, vol. 168, no. 3, pp. 209–232, 2005.

[137] M. Vladkov and J.-L. Barrat, "Local dynamics and primitive path analysis for a model polymer melt near a surface," *Macromolecules*, vol. 40, no. 10, pp. 3797–3804, 2007.

[138] J. Kalb, D. Dukes, S. K. Kumar, R. S. Hoy, and G. S. Grest, "End grafted polymer nanoparticles in a polymeric matrix: Effect of coverage and curvature," *Soft Matter*, vol. 7, no. 4, pp. 1418–1425, 2011.